Front. Optoelectron. 2017, 10(3): 211–238
DOI 10.1007/s12200-017-0718-4

REVIEW ARTICLE

Review of current methods of acousto-optical tomography for biomedical applications

Jacqueline GUNTHER (✉)[1], Stefan ANDERSSON-ENGELS[1,2]

1 Tyndall National Institute, Lee Maltings, Dyke Parade, Cork T12 R5CP, Ireland
2 Department of Physics, University College Cork, Cork T12 YN60, Ireland

© Higher Education Press and Springer-Verlag Berlin Heidelberg 2017

Abstract The field of acousto-optical tomography (AOT) for medical applications began in the 1990s and has since developed multiple techniques for the detection of ultrasound-modulated light. Light becomes frequency shifted as it travels through an ultrasound beam. This "tagged" light can be detected and used for focused optical imaging. Here, we present a comprehensive overview of the techniques that have developed since around 2011 in the field of biomedical AOT. This includes how AOT has advanced by taken advantage of the research conducted in the ultrasound, as well as, the optical fields. Also, simulations and reconstruction algorithms have been formulated specifically for AOT imaging over this time period. Future progression of AOT relies on its ability to provide significant contributions to *in vivo* imaging for biomedical applications. We outline the challenges that AOT still faces to make *in vivo* imaging possible and what has been accomplished thus far, as well as possible future directions.

Keywords acousto-optic, ultrasound modulation, optical imaging, biomedical imaging

1 Introduction

Near infrared optical imaging of biological tissue has good molecular contrast but poor spatial resolution and penetration depth, even under optimal conditions. Acousto-optical tomography (AOT) (also known as ultrasound-modulated optical tomography and ultrasound optical tomography) combines the spatial resolution of ultrasound imaging with the contrast of optical imaging [1]. AOT involves illuminating light through an ultrasound focus in a medium, where photons become "tagged" through a process described by the acousto-optic effect.

The acousto-optic effect has been known for nearly a century and was first theorized by Brillouin in 1922 [2]. In 1932, the acousto-optic effect was experimentally proven by Debye and Sears [3], as well as by Lucas and Biquard [4]. Conversely, AOT for biological imaging is a relatively new field that started in 1990s and has since gained attention. In 1993, Marks et al. introduced the possibility of using ultrasound to tag light to image homogeneous turbid medium [5]. Two years later, Wang et al. investigated continuous ultrasound modulation of laser light in tissue mimicking phantoms and obtained 2D images of objects buried in turbid media [6]. Then, Leutz and Maret developed a model that described one of the mechanisms behind ultrasound modulated light and tested their theory experimentally [7]. From there, many other techniques were introduced to aid in the detection of ultrasound modulated light, to understand the underlying mechanisms, and to study its limitations [1]. In 2001, the model developed by Leutz and Maret was modified by Wang to include an additional mechanisms of ultrasound modulated coherent light (see Section 2.2) [8].

Since the inception of AOT imaging for biological medium, the field has grown within the principal area of optical imaging and has incorporated its various methods. AOT has comparable optical contrast to diffuse optical tomography (DOT), another near-infrared imaging technique. In principle, AOT has better spatial resolution on the order of micrometres compared to DOT's millimeter resolution [9]. Optical coherence tomography (OCT) has very good spatial resolution (~10 μm), but lacks imaging depth that AOT can acquire [1,10]. Photoacoustic tomography (PAT) is another technique that combines optical and ultrasound imaging and has been an area of rapid expansion in the field. PAT sends a pulse of light and the ultrasound measures the thermoelastic expansion of the tissue. The contrast and spatial resolution of PAT is

Received March 31, 2017; accepted May 24, 2017

E-mail: jacqueline.gunther@tyndall.ie

comparable to AOT. Also, while PAT has become a more refined technique over the years, AOT has a couple of untapped advantages that can be explored in future development. For example, PAT is primarily sensitive to optical absorption properties, while AOT can be used to obtain absorption, scattering, and mechanical properties of tissue [9]. Additionally, AOT may have a larger potential imaging depth compared to PAT. Recently, Walther et al. investigated analytically the implementation of slow-light filters with AOT using the 1D diffusion approximation (DA) with extrapolated boundary conditions to determine the contrast-to-noise ratio (CNR) and found that AOT greatly outperform PAT, especially deeper within the tissue (~5 cm) [11]. AOT has not shown the rapid progress that PAT has exhibited, but has made interesting developments over the past six or seven years that has placed the field closer to *in vivo* applications.

One of the main challenges for AOT is that the ultrasound modulated light (tagged) signal is very small compared to the unmodulated light (untagged) signal. As a result, multiple detection schemes based on coherent light sources have been developed [1,9,10,12], including the ones that will be reviewed in this paper. The main goal for the AOT field has been overcoming the challenge of a low signal in the presence of a high background light level and developing a system that can obtain *in vivo* imaging. A secondary goal has been pushing the limits of imaging depth with optical systems with some groups achieving 9 cm or greater depths [13–16].

For this review, we aimed to explain the underlying physical phenomenon behind acousto-optical interactions in biological medium. Moreover, we present here a current overview of AOT advancements since around 2011. We have chosen to make the review rather extensive with the aim to include all publications to our knowledge in the area since the last two reviews within the field [10,12]. In closing our review we also take the liberty to select our subjective highlights of the field within the last years and envision future directions. This section may be used as one set of recommendations deserving a closer study. We have divided the review according to the following topics:

- Basic concepts of
  - o Photon tagging
  - o Underlying mechanisms of AOT
  - o Using simulations to further understand acousto-optical interactions
- Review of the recent work accomplished on instrumentation development of
  - o The ultrasound side of AOT
  - o The optical side of AOT
  - o Combination with PAT
  - o Commercial products
- Types of reconstruction algorithms that have been established.
- Discussion
  - o The main challenges of the field
  - o Subjective highlights of the field
  - o Future direction of the field

2 Basic concepts

In this section, the theoretical basis for the acousto-optical technique is formulated. The text is divided in three parts, describing the concept of light-ultrasound interaction, how this can be quantified through a few different mechanisms, and finally how one can model ultrasound modulated light.

2.1 Light "tagging"

The output of a sufficiently coherent light source traveling through a medium is a speckle pattern (see Fig. 1(a)). The speckle pattern is caused by the phase difference of the light that took different paths of varying lengths through the medium. Ultrasound modulation causes accumulations of phase changes of the light due to various mechanisms (see next section). The added time-varying process of ultrasound perturbation causes the speckle pattern to change quicker, which causes a blurring effect when imaged (see Fig. 1(b)) [12].

When light passes through an ultrasound beam, the light is phase modulated such that the frequency spectrum displays sidebands at multiples of the modulation frequency in which $\nu_s = \nu_0 \pm \nu_a$, where ν_0 [Hz] is the unmodulated light frequency, ν_a [Hz] is the acoustic frequency, and ν_s [Hz] is the frequency of the side-bands (see Fig. 1(c)) [11,12]. The fraction of the modulated light signal is very small compared to the background light. As a result, the amount of modulated light determines the signal-to-noise ratio (SNR), the signal-to-background, and the thickness of tissue that can be imaged [17].

Tagging efficiency, or modulation efficiency describes what fraction of the light is frequency shifted within the ultrasound focus. Since the light is being scattered multiple times at various angles and can undergo multiple passes within the ultrasound foci, the average modulation efficiency is calculated with a simple model. Modulation efficiency (η [−]) is dependent on the incident angle (θ [rad]) of the light into the focus based on Raman-Nath theory (up to θ_{max}). The average modulation efficiency can be determined using $\eta_{avg} = \int_0^{\theta_{max}} \eta(\theta) d\theta / \theta_{max}$ [18]. Tagging efficiency was found to be independent of scattering coefficient (within biological relevant range) for high ultrasound pressure when particle displacement is greater than 1 nm [19].

2.2 Mechanisms

There are three proposed mechanisms for the frequency shift of light due to the modulation of ultrasound [8]. Simple models for these three mechanisms will be briefly

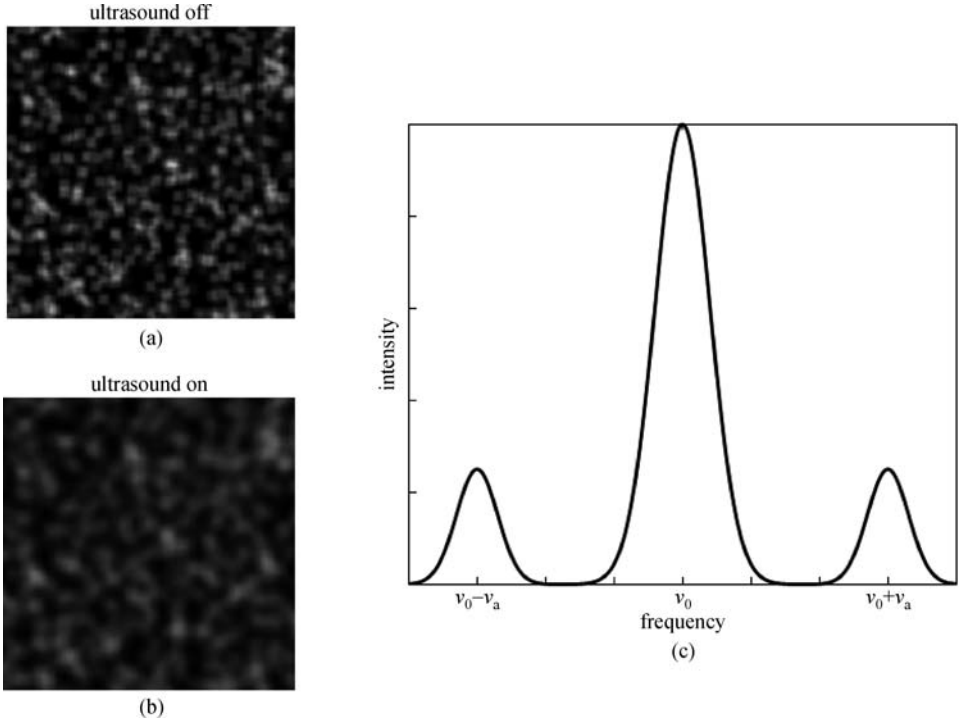

Fig. 1 (a) Mock speckle pattern generated to demonstrate signal with the ultrasound perturbation off. (b) A mock speckle pattern with the ultrasound perturbation on. (c) Example of frequency spectrum of output signal from light tagging in which there is the optical frequency (ν_0) and the side-bands shifted ± the ultrasound frequency (ν_a)

described below to facilitate the understanding and to provide the tools to mathematically simulate the dependence of various parameters. The first mechanism is a change in phase variations due to the movement of scatterers under ultrasound perturbation. This mechanism was proposed by Leutz and Maret [7], who modeled the phase variation of light caused by the displacement of scatters (see Fig. 2(a)). This was under the assumption that the mean free path was much greater than the acoustic wavelength [7]. The second mechanism is the change in phase variations due to the change in the index of refraction between scattering events (see Fig. 2(b)). The third mechanism is caused by the variation in density due to the ultrasound perturbation which in turn causes changes in the absorption and scattering properties (see Fig. 2(c)). The third mechanism does not require a coherent light source, while incoherent ultrasound modulated light has a very weak signal [8,20]. There have been studies that detect these weak incoherent light signals [21–23].

Wang combined the first two mechanisms involving coherent light to create an analytical model for ultrasound modulated coherent light in scattered media [8]. The autocorrelation function of the electrical field at the detector (G) was obtained by first deriving the phase shift due to displacement of scatterers, $\Delta\phi_d$ and the phase shift due to change in refractive index, $\Delta\phi_n$. The model consists of a plane ultrasound wave through a homogenous medium in which the ultrasound amplitude (A) was much smaller than the wavelength of light ($A \ll \lambda_0$) and the mean free path (mfp) between light scattering events is much larger than the optical wavelength (mfp $\gg \lambda_0$).

Phase variation of the detected light due to the displacement of scatterers in the medium by the ultrasound is represented by

$$\phi_{dj} = -n_0 k_0 \left(\hat{\boldsymbol{k}}_{j+1} - \hat{\boldsymbol{k}}_j\right) \cdot \boldsymbol{A} \sin(\boldsymbol{k}_a \cdot \boldsymbol{r}_j - \omega_a t), \qquad (1)$$

where n_0 [−] is the background index of refraction, k_0 [m^{-1}] is the amplitude of the optical wave vector, $\hat{\boldsymbol{k}}_j$ [m^{-1}] is the unit optical wave vector at the jth scattering event, $\boldsymbol{A}$ [m] is the acoustic amplitude vector, $\boldsymbol{k}_a$ [m^{-1}] is the ultrasound wave vector, $\boldsymbol{r}_j$ [m] is the vector for the location of the jth scattering event, ω_a [Hz] is the angular frequency of the ultrasound, and t [s] is time.

The phase variation due to local change in index of refraction due to the ultrasound was modeled by

$$\phi_{nj}(t) = 2\eta_0 \eta k_0 A \sin(\boldsymbol{k}_a \cdot \boldsymbol{r}_{j-1} + k_a l_j \cos\theta_j/2 - \omega_a t) \times \sin(k_a l_j \cos\theta_j/2)/\cos\theta_j, \qquad (2)$$

where η [−] is a coefficient related to the adiabatic piezo-optic coefficient ($\delta n/\delta P$) of the material so that $\eta = \delta n/\delta P \rho v_a^2$, in which P is pressure [N/m^2], ρ is density [kg/m^3] and acoustic velocity is v_a [m/s]; l_j [m] is the jth path length, and θ_j [rad] is the angle between the optical wave vector of the jth free path. Equation (2) was derived from $\phi_{nj}(t) = \int_0^{l_j} k_0 \Delta n(\boldsymbol{r}_{j-1}, s_j, \theta_j, t) \mathrm{d}s_j$.

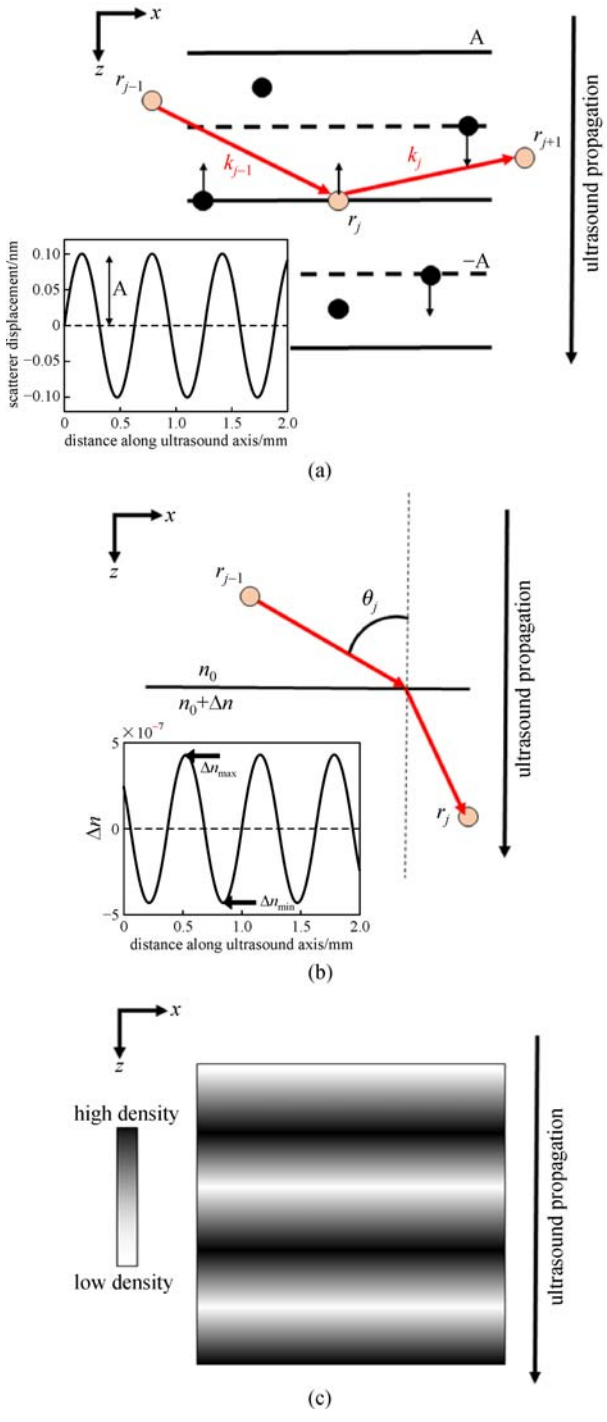

Fig. 2 Two coherent mechanisms that contribute to phase change in ultrasound modulated light. (a) Phase change due to the displacement of scatterers in which light scatters off of moving particles within the ultrasound beam and causes a change in direction. Inset shows scattering displacement of an ultrasound wave with amplitude A. (b) Refraction of light between two scattering events due to changes in index of refraction. Inset shows Δn along the ultrasound axis. (c) The third mechanism involving incoherent light propagation. The ultrasound perturbation causes a change in the density of the medium, which causes a change in the optical properties

The autocorrelation function of the electric field was determined using

$$G(\tau) = \int_0^\infty p(s)\langle E_s(t)E_s^*(t+\tau)\rangle \mathrm{d}s, \tag{3}$$

where $\langle\ \rangle$ denotes averaging over time t, E_s [V/m] is the electric field of the scattered light of path length s [m], and $p(s)$ [−] is the probability density function of s. The autocorrelation function has contributions from both Brownian motion and the ultrasound, but these contributions are independent and have different cut-off frequencies. Only the ultrasound portion was considered here. The ultrasonic contribution to the autocorrelation function by s/l events along path s is

$$\langle E_s(t)E_s^*(t+\tau)\rangle = \left\langle \exp\left\{ -i\left[\sum_{j=1}^{\frac{s}{l}+1}\Delta\phi_{nj}(t,\tau) + \sum_{j=1}^{\frac{s}{l}}\Delta\phi_{dj}(t,\tau)\right]\right\}\right\rangle, \tag{4}$$

where l is the transport mean free path.

After some derivation the analytical solution is [1,8,24]

$$G(\tau) = \frac{\left(\frac{L}{l}\sinh\left[\{\varepsilon[1-\cos(\omega_a\tau)]\}^{\frac{1}{2}}\right]\right)}{\sinh\left[\frac{L}{l}\{\varepsilon[1-\cos(\omega_a\tau)]\}^{\frac{1}{2}}\right]}, \tag{5a}$$

$$\varepsilon = 6(\delta_n + \delta_d)(n_0k_0A)^2, \tag{5b}$$

$$\delta_n = (\alpha_{n1} + \alpha_{n2})\eta^2, \tag{5c}$$

$$\alpha_{n1} = \frac{k_a l\tan^{-1}(k_a l)}{2}, \tag{5d}$$

$$\alpha_{n2} = \frac{\alpha_{n1}}{\frac{k_a l}{\tan^{-1}(k_a l)} - 1}, \tag{5e}$$

$$\delta_d = \frac{1}{6}. \tag{5f}$$

The contribution from the displacement parameter of scatterers δ_d [−] is independent of $k_a l$. While, the contribution from the change in index of refraction δ_n [−] increases with $k_a l$ (see Figs. 3(a) and 3(b)). Additionally, there are two parts of δ_n: α_{n1} and α_{n2}. The component α_{n1} [−] increases with $k_a l$, since a "longer free path relative to the acoustic wavelength accumulates a greater phase modulation." The component α_{n2} [−], on the other hand, slightly decreases due to counteracting effects in which α_{n1} increases, but the denominator increases due to decrease coupling of the free paths (see Figs. 3(c) and 3(d)). Therefore, as the frequency of ultrasound increases

the phase variation due to change in index of refraction becomes the dominating factor in the modulation depth measurements [8].

An example of the autocorrelation function can be seen in Fig. 4(a). The Fourier transform of G yields a modulation spectrum and has a peak at the ultrasound frequency (see Fig. 4(b)). Using the Wiener-Khinchin theorem the light intensity with frequencies $n\omega_a$ from the unmodulated light frequency ($n = 0$) can be calculated with

$$I_n(n\omega_a) = \frac{1}{T_a}\int_0^{T_a} \cos(n\omega_a\tau)G(\tau)\mathrm{d}\tau, \tag{6}$$

where T_a [s] as the ultrasound period (Fig. 4(c)). Equation (6) shows the intensity of the frequency spectrum of G at the ultrasound frequency ($n = 1$) and at each harmonic ($n > 1$). Then the modulation depth, $M = I_1/I_0$ can be calculated. The modulation depth describes the ratio of the intensity of the light after being shifted one ultrasound frequency compared to the unmodulated light [1,8,20]. When only phase variation due to the displacement of scatterers is considered, the modulation depth does not vary as k_a increases because the average phase accumulation is not dependent on k_a. Modulation depth does increase with k_a for phase variation due to index of refraction since the average phase accumulation increased with k_a (Fig. 4(d)) [20]. Wang used this analytical solution to modify an existing Monte Carlo algorithm to simulate photon propagation and determine phase change of light under the influence of continuous ultrasound perturbation in non-absorbing homogeneous isotropic medium [20]. Thereafter, the model was further extended to account for anisotropic medium [25], inhomogeneous scattering medium [26], focused ultrasound [27,28], and pulsed ultrasound [28,29].

2.3 Simulating ultrasound modulated light

Using Wang's Monte Carlo (MC) model [20] and the graphics processing unit (GPU) based MC code Compute Unified Device Architecture Monte Carlo for multi layered tissue (CUDAMCML) [30], Leung and Powell created a GPU MC simulation of ultrasound modulated light [31]. Their MC code matched the analytical model [25] and was faster than the CPU version. Additionally, they developed a method to acquire the speckle pattern caused by ultrasound modulation. The MC for AOT could easily incorporate new mechanisms and runs at a reasonable speed (~10 min) [31]. The code was further developed for inhomogeneous medium with designated ultrasound regions [32].

Since acoustic propagation is dependent on mechanical properties of the medium (i.e., density, viscosity, etc.), groups have combined mechanical models with MC for AOT. Adams et al. combined models for acoustic field using the angular spectrum method, temperature field

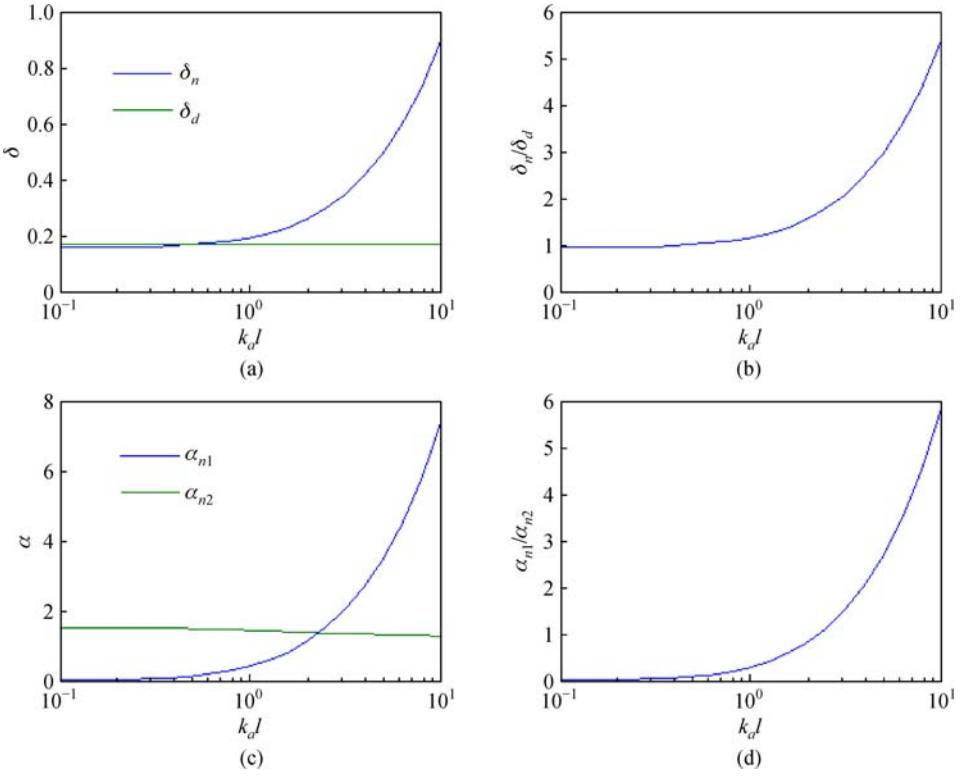

Fig. 3 (a) Parameters δ_n and δ_d of the autocorrelation function versus $k_a l$. (b) The ratio of δ_n/δ_d compare to $k_a l$. (c) Change in α_{n1} and α_{n2} and (d) ratio of α_{n1}/α_{n2} versus $k_a l$. Recreated from Ref. [8]

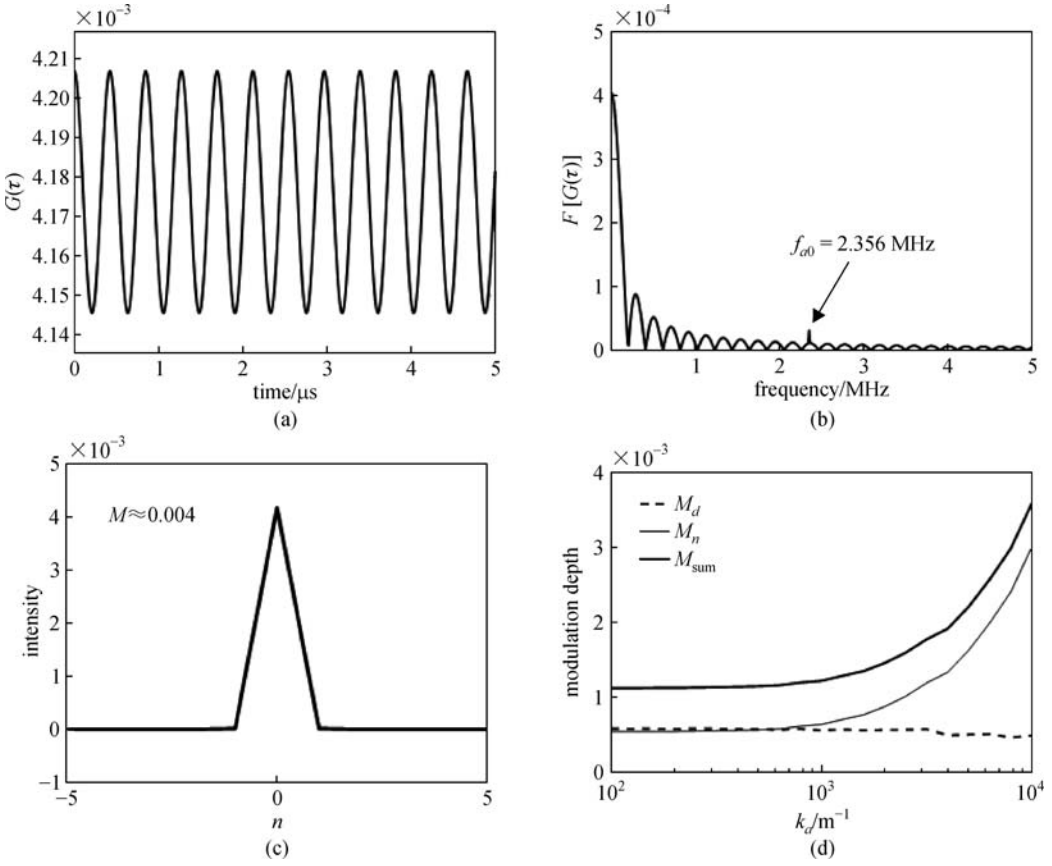

Fig. 4 Using Eqs. (5) and (6), from the analytical model in which $A = 0.1$ nm, $v_a = 1480$ m/s, $\rho = 1000$ kg/m^3, $\delta n/\delta p = 1.466\text{E}-10$ m^2/N, $n_0 = 1.33$, $\lambda = 500$ nm, $\mu_s = 10$ cm^{-1}, $L = 5$ cm, and $k_a = 10000$ m^{-1}. Parameters were taken from Refs. [8,20]. (a) An example of the autocorrelation function (G). (b) Fourier transform of G with one of the peaks corresponding to the acoustic frequency f_{a0}. (c) Example of $I_n(n\omega)$ as a function of n (integer) in which the modulation depth in the example is $M\approx0.004$. (d) Modulation depth with respect to k_a with only the displacement component (M_d), only the index of refraction component (M_n), and both components (M_{sum}) considered. Modulation depth was calculated analytically and recreated from Refs. [12,20]

using a finite-different time-domain solution to the Pennes bioheat equation, and light propagation using MC to determine design parameters for high intensity focused ultrasound acousto-optic guided system [33]. There have been MC simulations developed to study light modulation caused by acoustic radiation force induced shear waves [34–36]. Also, there have been MC simulations that combine the effects of Brownian motion, ultrasound modulation, and blood flow [37,38].

Through computational modeling, Hollmann et al. showed that focusing in turbid medium can be improved with the ultrasound focus as a guidestar and phase conjugation. Finite difference time domain (FDTD) models were used on Maxwell's equations. Their 2D models displayed spatially coherent optical channels. However, these optical channels are not well understood in 3D and optical channels for different 2D simulations behave differently depending on the scattering structures, densities, and depth of the medium [39]. They also used FDTD methods to develop a diffusion model to determine reflectance of the modulated diffusive wave [40].

3 Instrumentation and techniques

There are two aspects of AOT that can be manipulated to achieve the desired design parameters: the ultrasound and optical setups. There has been sufficient effort to utilize different ultrasound techniques to improve the acousto-optical signal or use acousto-optical imaging to determine the mechanical properties of a medium. On the other side, there has been work that has focused on optical techniques with similar goals to increase SNR or decrease time. Last, a couple of commercial systems have been developed for acousto-optical imaging of the brain. We will discuss all these concepts in more detail in the following sections. See Table 1 for a summarization of the techniques.

3.1 Ultrasound techniques

The parameters of ultrasound perturbation have an effect on the modulation efficiency of light. For example, experimental results have shown that modulation efficiency increases as you increase the pulse energy (0 – 100

Table 1 Summarization of AOT approaches and impact

area	technique	approaches	challenge(s) addressed	Ref.
ultrasound	dual ultrasound frequencies	two ultrasound foci	speed	[41]
		two-region transducer	determine Young's modulus	[42–44]
		two ultrasound transducers	axial resolution	[45]
	pressure contrast	different pressure waves	determine scattering coefficient	[46,47]
	second harmonic	ultrasound pulse sequences	resolution and SNR	[48–50]
	planar waves	combined with image reconstruction	speed	[51]
	HIFU	combined AOT and HIFU	monitoring HIFU	[47,52]
	microbubbles	TRUME; pulsed laser speckle contrast detection; fluorescent microbubbles	resolution and contrast	[53–55]
	acoustic radiation force	laser-speckle contrast analysis	track shear waves and estimate mechanical properties	[36,56–60]
optical	speckle contrast and modulation depth measurements	parallel speckle detection; speckle contrast; nanosecond laser pulses	obtaining modulated light measurements from speckle pattern	[61–65]
	incoherent light sources	LED light source; imaging chemiluminescent source; bioluminescence numerical model; fluorescent objects	observation of incoherent ultrasound modulated light	[21–23,66]
	interferometry and heterodyne holography	CMOS smart pixel array and FT-AOI; lock-in camera	amplification of unmodulated light signal without background amplification	[67–69]
	photorefractive crystal based detection	$Sn_2P_2S_6$:Te crystal; ND:YVO_4 crystal; $Bi_{12}SiO_{20}$ crystal; high numeric aperture fiber bundle; photorefractive polymer	detection of modulated or unmodulated light signal	[15,16,70–74]
	phase conjugation with photorefractive crystals and polymers	TRUE with $Bi_{12}SiO_{20}$ crystal, photorefractive polymer, or $Sn_2P_2S_6$:Te crystal, SLM	focus phase conjugated beam within a medium	[18,75–80]
	focused fluorescent excitation	TRUE; combining SLM-based illumination and PRC-based detection; digital phase conjugation; TROVE light; iTRUE	fluorescent imaging beyond the ballistic regime (~1 mm)	[81–88]
	quantum memory techniques	spectral hole burning; atomic frequency comb	filter sidebands of signal spectrum	[14,89–92]
misc.	acousto-optical coherence tomography	continuously applied light and ultrasound with random phase jumps	resolution and SNR	[93–96]
	combined with PAT	assist AOT:PAT guided ultrasound wavefront shaping	compensate for speed of sound aberrations	[97]
		assist PAT:measuring fluence with AOT	compensate for fluence variations in PAT signal	[19,98,99]
	commercial	acquire dynamic blood flow measurements	clinical trials in humans	[100–102]

μJ) of ultrasound, while pulse repetition frequency has no effect on the signal. Additionally, the spectral intensity of the ultrasound modulated signal was found to be higher for a 1 MHz ultrasound pulse compared to 2.25, 5, or 10 MHz [103]. However, ultrasound techniques are not limited to simply changing the frequency or power. Ultrasound imaging is a large field that can provide a plethora of techniques, and as a result, AOT has benefited from the groundwork that has been done in conventional ultrasound research. Here, we present in more detail the several configurations of AOT systems that have employed different ultrasound techniques to improve imaging and bring it closer to *in vivo* applications. Generic methods are schematically illustrated in Fig. 5.

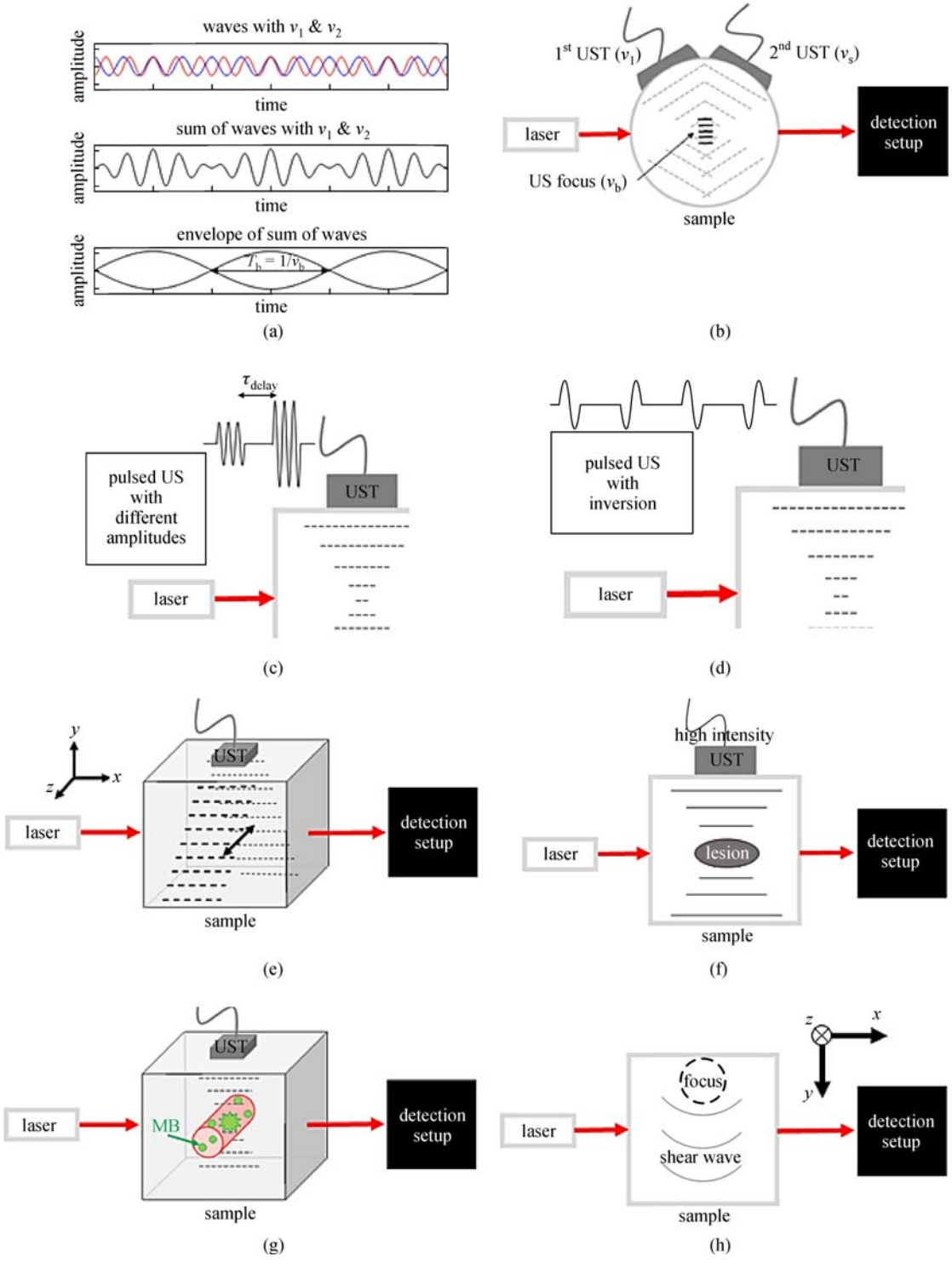

Fig. 5 Examples of concepts and generic configurations of the ultrasound portion of AOT. (a) Example of two frequencies (ν_1 and ν_2) forming a beat frequency (ν_b) with period T_b. (b) An ultrasound focus caused by two ultrasound transducers (UST) with beat frequency ν_b. (c) AOT configuration with two ultrasound (US) pulses of different pressure. (d) Pulse sequencing with inverted ultrasound pulses. (e) Planar wave imaging where the laser input is in the x-direction, ultrasound is propagating in the negative y-direction, and then the ultrasound is swept in the z-direction. (f) High intensity focused ultrasound (HIFU) used to create a lesion in the medium. (g) Imaging with microbubbles (MB) in which the microbubbles are destroyed with ultrasound which causes a change in the electric field that is detected. (h) An example of acoustic radiation force (ARF) imaging. Ultrasound propagation is in the z-direction. A shear wave propagates perpendicular (y-direction) to the ultrasound propagation. Laser light is illuminated through the shear wave (x-direction)

3.1.1 Dual ultrasound frequencies to gain speed, mechanical properties, or resolution

One of the methods that has been investigated has been the use of two ultrasound frequencies to assist with acousto-optical imaging in order to increase speed, extract mechanical properties of the tissue, or increase axial resolution. This dual frequency technique can be accomplished in several ways, such as delaying two ultrasound pulses of different frequencies, using a confocal two-region ultrasound transducer, or simply adding another ultrasound transducer.

Fiolka et al. employed a single ultrasound transducer to sequentially create two foci in the medium at different depths with different carrier frequencies. The double foci was achieved by sending two ultrasound pulses (2 Hz frequency difference) with a short time delay (33 ns). Once the first focus passed the center of the medium, the laser (778 nm) pulse arrived [41]. Fluorescence images were captured using a digitally optical phase conjugation focusing methods similar to the approaches used by Si et al. and Cui and Yang [81,104] (see Figs. 6(e) and 6(f) for generic setup). The wavefronts from each focus was phase conjugated in sequence and detected. Using one or two ultrasound foci had no effect on the SNR, but the imaging could be made faster with multiple ultrasound foci employed. The limiting factor was the switching speed of the spatial light modulator (SLM), which was about 0.1 s. Increasing the speed of AOT imaging is an important challenge to overcome, since the overall goal of this technique would to be able to imaging *in vivo* which has an intrinsic decorrelation time of about 1 ms [41].

Chandran et al. recovered the Young's Modulus of tissue phantoms utilizing acousto-optical imaging techniques with a confocal two-region transducer. This transducer could probe the medium with two ultrasound frequencies (ν and $\nu+\Delta\nu$) so that the forcing frequency was the beat frequency ($\Delta\nu$) (see Fig. 5(a)). By changing the frequencies, the resonance of the region of interest could be found, which also corresponds to the peak modulation (M) measurement. The modulation measurement at the resonance frequency had a higher SNR than the non-resonance frequencies. Also, Young's Modulus can be related to the resonance of a material and therefore was calculated [42]. Using similar acousto-optical imaging techniques combined with diffuse wave spectroscopy, Chandran et al. used the technique to measure the decay in the modulation depth (M) and amplitude of intensity of the autocorrelation function (G) of liquid flow in a tissue phantom, which can be related to the mean-square displacement of scatterers [43,44]. They observed that the decay rate was faster for modulation depth compared to autocorrelation. However, their estimates of flow through the medium were underestimated by $\sim 1-2$ orders of magnitudes. The discrepancies were attributed to super-diffusive dynamics that were not taken into consideration [43]. Singh et al. used Monte Carlo simulations and phantom studies to observe the effects of the average phase variations at different beat ultrasound modulation frequencies in AOT. When the beat frequency was over about 1 kHz and especially at 1 MHz, the average phase was about zero for both simulations and phantom measurements. The nonzero average phase could be used to determine localized index of refraction within a medium [105].

A beat frequency could, as described above, be obtained with two ultrasound transducers set to different frequencies and was implemented by Yang et al. to increase the axial resolution [45]. The transducers were added to one of their previous photorefractive-based detection configurations of the imaging method [75]. The light was modulated at the beat frequency of the two ultrasounds where the foci intersected (see Fig. 5(b)). They were able to improve the axial resolution by 2.4 times to 1.1 mm [45].

3.1.2 Pressure contrast to gain info on scattering coefficient

Another ability of ultrasound is to vary the amplitude of the signal and create different pressure waves. Lai et al. used a photorefractive crystal (PRC) based interferometer system (see Fig. 6(c) for generic setup) to observe AOT with varying pressure amplitudes. Two ultrasound pulses at three cycles each with pressures at 0.3 and 1.5 MPa were generated and emitted 96 μs apart (see Fig. 5(c)). These different pressure waves were able to produce different optical output intensities. The ratio of these two intensities can be related to the scattering coefficient within the medium. They were able to calculate the pressure contrast signal (PCS) that they define as

$$PCS=\frac{I_S^{P^{f1}}}{I_S^{P^{f2}}}=\frac{\sum_{j=1}^{n}[1-J_0(|\beta P_j^{f1}|)]}{\sum_{j=1}^{n}[1-J_0(|\beta P_j^{f2}|)]}, \tag{7}$$

where I_s [W/m^2] is the acousto-optical intensity at peak focal pressures P^{f1} [N/m^2] and P^{f2}, J_0 is the zeroth order Bessel function, j [m] is the propagation path through the interaction region, and β [N$^{-1}\cdot$m^2] was a function of the mean free path. The product of β and the pressure (P_j) gives the phase shift (Φ_j) that had been accumulated over path j. The PCS was shown to be independent of characteristics of the detection system and the amount of modulated light detected. Additionally, PCS can be related to the mean free path of the light (the inverse of the scattering coefficient), which means that quantitative measurements of the media can be acquired [46,47].

3.1.3 Ultrasound pulse sequences and second harmonic to gain resolution and SNR

Another way to implement acousto-optical imaging techniques has been utilizing ultrasound pulse sequences and second harmonic ultrasound. To obtain the second

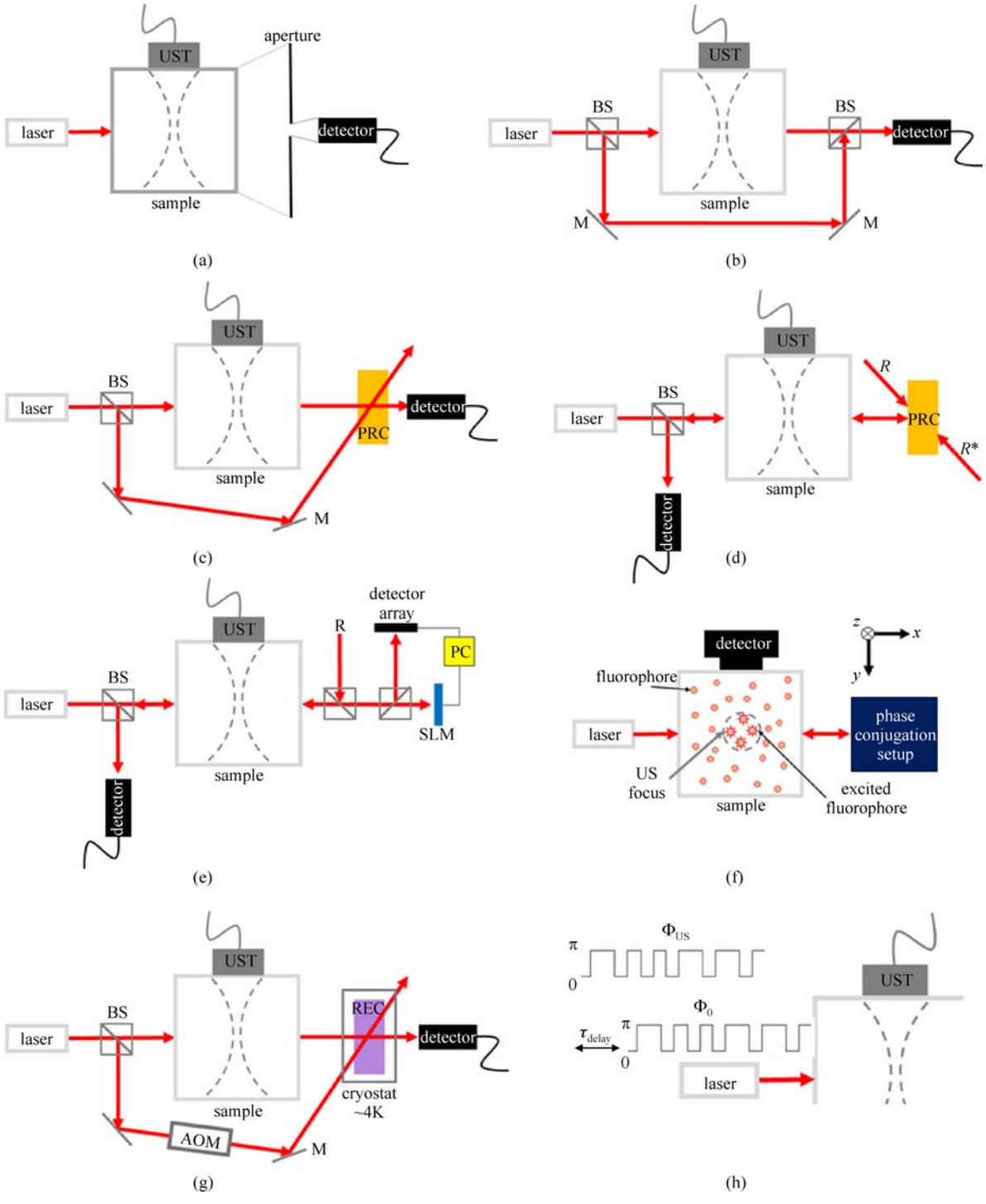

Fig. 6 Generic examples of optical configurations that have been utilized or developed. Each setup consist of laser illumination that travels through a sample that undergoes ultrasound perturbation. (a) Speckle imaging. (b) Heterodyne digital holography, which can be configured with an acousto-optic modulator so that the reference beam matches the tagged or untagged photons (untagged shown). (c) Photorefractive crystal based interferometry. (d) Phase conjugation with photorefractive crystals (PRC). (e) Phase conjugations with spatial light modulator (SLM). The signal from the sample is detected with detector array, which is processed with the PC, and displayed on the spatial light modulator. The reference beam reflects off the SLM and back into the sample where it is refocused into the ultrasound focus and detected. (f) Fluorescent imaging. Ultrasound propagation is in the z-direction. The light is illuminated through the ultrasound focus and the sample. The light is phase conjugated back and then detected. Detector can be placed on a different surface of the sample. (g) Spectral hole burning in a rare-earth crystal (REC). The crystal is first burned with a reference beam that had been tuned to the tagged photon frequency. Then the signal is transmitted through the sample and the tagged photons that pass through the REC are detected. (h) Acoustic optical coherence tomography. The ultrasound signal undergoes random phase jumps (Φ_{US}) between 0 and π. The laser light is also amplitude modulated and undergoes the same random phase jumps (Φ_0) as the ultrasound but with a time delay (τ_{delay}). UST: ultrasound transducer, US: ultrasound; BS: beam splitter, M: mirror, PRC: photorefractive crystal, R: reference, R*: conjugate of reference beam, SLM: spatial light modulator, PC: personal computer, AOM: acousto-optical modulator, REC: rare-earth crystal

harmonic in ultrasound imaging, the detected ultrasound pulse and detected inverted ultrasound pulse are summed which cancels out the fundamental frequency and retains the second harmonic. There is greater harmonic generation in material with high nonlinear parameters such as tissue and tissue mimicking gels [48].

The same technique was used by Ruan et al. to employ the ultrasound second harmonic in AOT imaging. They created a pulse sequence of ultrasound pulses followed by its inversion (see Fig. 5(d)). The sequence was repeated at a phase shift of the ultrasound pulse ($0 \rightarrow \pi/2$). Optical pulses were also applied after the ultrasound ones and the phase modulated speckle pattern was acquired. Lateral resolution was improved and sufficient axial resolution was achieved due to ultrasound pulses [48]. To further develop the technique, a series of ultrasound pulses followed by its inverted counterpart with synchronized optical pulses were used to produce a detection response similar to a lock-in amplifier. This second harmonic lock-in technique improved the lateral resolution but at the expense of SNR [49]. Ruan et al. then developed a lock-in parallel speckle detection technique that can also detect ultrasound modulated light. The multipixel detection of this approach allowed for time gating along the acoustic axis and optimized the SNR [50].

3.1.4 Planar ultrasound waves to gain acquisition speed

One of the time dependent factors of acousto-optical imaging speed is the number of ultrasound pulses needed to acquire an image. Laudereau et al. used ultrasound plane waves (see Fig. 5(e)) and a reconstruction code to decrease the number of pulses by 50 times, while retaining the same SNR. The system used PRC-based detection (see Fig. 6(c) for generic setup). The plane waves were able to modulate more light waves than a focused beam. They measured the mechanical index (MI), an ultrasound safety parameter. The MI was 0.43, which is way below the FDA limit (1.9) and even those typically used in the focused beam (1.14). This means that the ultrasound power could have been further increased which would consequentially increase the acousto-optical signal. Additionally, the transducer was fixed instead of being translated along an axis. Last, the reconstruction method was similar to one employed for CT scans and was a filtered back-projection method for acousto-optical imaging. The reconstructed image was distorted in the lateral direction at the high imaging rate. To correct for this effect, they added a second transducer perpendicular to the first, which greatly improved the quality of the image [51].

3.1.5 High intensity focused ultrasound monitoring

Ultrasound can also be employed for therapeutic applications. High intensity focused ultrasound (HIFU) noninvasively induces damage in tissue and could be used for applications such as tumor treatment. Estimating the intensities of HIFU is difficult due to the heterogeneous nature of biological tissue. Therefore, acousto-optical imaging could be used for real-time monitoring of the effects within the ultrasound focus to improve safety and efficiency. Lai et al. used an acousto-optical imaging system with PRC-based interferometry (see Fig. 6(c)), where the ultrasound transducer was used to modulate the light signal and provide the lesion formation (see Fig. 5(f)). Lesions were not visible in their ultrasound B-mode scan nor were any cavitation detected. However, as HIFU was applied, the acousto-optical signals decreased. The change in the normalized acousto-optical signals was proportional to the lesion size regardless of ultrasound exposure parameters. The system was set up in transmission geometry and was not optimized for *in vivo* treatment. They performed real-time measurements with 7 frames a second [47,52]. Recently, Adams et al. developed a numerical model combining effects of the acoustic fields, temperature fields, and light propagation to optimize the design for a HIFU AOT system [33].

3.1.6 Microbubbles to gain resolution and SNR

Another ultrasound tool combined with AOT was microbubbles, which are commonly used to increase ultrasound contrast by taking advantage of the high acoustic signals generated in the tissue-microbubble interfaces due to nonlinear effects. To increase the spatial resolution of ultrasound-modulated optical imaging, Ruan et al. incorporated microbubbles with AOT [53]. Their technique was called time-reversed ultrasound microbubble encoded (TRUME) optical focusing. Ultrasound was used to destroy microbubbles which created a different optical field compared to the unmodulated sample (see Fig. 5(g)). The difference of these two images was obtained and phase conjugated back into the sample. With a single microbubble, a resolution of ~2 μm was achieved. In the presence of many microbubbles the resolution was half the size of the ultrasound focus. The TRUME system had a peak-intensity to background ratio (PBR) of ~510 which was much higher than the time-reversed ultrasonically encoded optical focusing system (~2). The TRUME system also creates an optical focus in about 280 ms, which would be viable for *ex vivo* studies and some *in vivo* studies. Microbubbles, while an invasive technique, have been widely used in ultrasound imaging and have the potential to be incorporated for drug delivery or established as molecular markers [53].

By combining microbubbles and a pulsed laser speckle contrast detection technique, Ruan et al. was able to improve the contrast in acousto-optical imaging [54]. Their system was setup to determine speckle contrast. Their improvement in contrast was contributed to microbubble destruction. The authors admit that this technique was not as efficient as their pulse inversion technique [48] with

regards to separating the fundamental and second harmonic frequencies. This technique does not require phase stepping, which give the advantages of decreasing the effects of speckle decorrelation and also providing a detection setup with high etendue [54].

Liu et al. developed a technique to image fluorescent microbubbles. The ultrasound waves causes fluctuations in the microbubble diameter, which in turn, varies the fluorophore density on the surface of the microbubble. The fluorescent signal then increases or decreases depending on these fluctuations. The fluorescence signal was detected with a photomultiplier tube. This method had high temporal (< 1 μs or < 1 ns) and spatial resolutions (< 1 μm) [55]. These methods modulate the fluorescent microbubbles signal, not the frequency of the laser light. This is thereby a bit out of the scope of this review, but worth noting since the system setup is similar to other groups and could easily be employed as an additional method of imaging for further information.

3.1.7 Acoustic radiation force to obtain shear wave velocity, elasticity, and viscosity

Last, one group studied the use of acoustic radiation force (ARF) with AOT. ARF is the unidirectional force that is generated within a medium exposed to ultrasound. The force is caused by the small momentum transfer between the transducer and the medium. ARF causes greater tissue displacement of a few micrometre compared to ultrasound, which is typically in the nanometre range. By increasing the displacement of scatters in the medium, a greater modulation depth could be achieved. One of the effects of ARF are shear waves that move perpendicular to the direction of the ultrasound [12]. The ARF can be used in acousto-optical imaging to increase the signal by increased modulation of the light waves. Li et al. discovered that by optimizing the exposure time of the detector, the effect of the shear wave can be minimized [56]. They were able to increase the contrast by 110% and the spatial resolution was improved by 40%. The system composed of a laser light passing through a phantom that was exposed to ultrasound and detected with a CCD camera (see Fig. 5(h)). The signal with and without the ultrasound was compared to produce the acousto-optical signal [56]. Using ARF and AOT techniques, the shear wave propagation can be tracked and the velocity estimated. This can possibly be a tool for non-invasive measurements of tissue elasticity *in vivo* (1.2 cm depth) [57]. Additionally, these techniques can also be used to determine viscosity at centimeter depths in tissue phantoms [58].

Li et al. developed models to track shear wave propagation by using laser-speckle contrast analysis. These models were incorporated into MC simulations and compared to experimental results. The speckle contrast was tracked over time to observe the effect of the shear wave moving through the medium. As the shear wave passes the optical detection zone, there is an increase in the signal due to more light being modulated in that region. The time trace of the speckle contrast was used to determine the speed of the shear wave. Also, they observed an increase in contrast as the shear wave amplitude increased [36].

Cheng et al. continued to build on their ARF system and created a combined shear-wave laser speckle contrast analysis (SW-LASCA) and ARF-assisted ultrasound modulated optical tomography system. They were capable to quantitatively measure the elasticity of tissue phantoms and qualitatively resolve absorption information at centimeter depths [59]. Using these methods, multiple shear waves were observed and their interactions studied. Dual counter-propagating shear waves allowed for more accurate measurements to shear wave speed due to higher contrast and sharper peaks due to constructive interference of the waves. Additionally, there was less boundary effects with two waves compared to one. Although the speckle decorrelation does not affect the time of flight of the acousto-optical imaging signal as the shear wave passes, it can decrease the SNR [60].

3.2 Optical techniques

Congruent with the development of ultrasound techniques, there have been many different optical methods implemented to extract better acousto-optical signals. Here, we present the instrumentation and phantom studies undergone to improve optical methods for AOT. Generic methods are schematically illustrated in Fig. 6.

3.2.1 Speckle contrast and modulation depth measurements

Since ultrasound modulation causes a shift in the frequencies of some of the input light, the speckle pattern of the light exiting the tissue will be altered. There have been methods that have been developed to analyze this altered speckle pattern. One method has been based on parallel speckle detection. For this method, the speckle pattern is imaged at different phase delays between the signals sent to the ultrasound transducer and the amplitude modulated laser. For example, four acquisitions with phase delays of 0°, 90°, 180°, and 270° could be acquired. The DC and AC components of the signal can be calculated and the modulation depth determined. This can also be accomplished with less than four different phase delays to decrease acquisition time [61]. The technique can be sensitive to speckle decorrelation due to the long acquisition time [106].

Another technique has compared speckle pattern with and without ultrasound perturbation. Under ultrasound modulation, a blurred speckle pattern can be observed with the requirement that the exposure time of the detector is

shorter than the speckle decorrelation time. Speckle contrast C is calculated using

$$C(z) = \frac{\sigma}{\langle \bar{I} \rangle}, \tag{8}$$

where z [m] is the axial distance, σ [W/m^2] is the standard deviation of the measured light intensity for each camera pixel, and $\langle \bar{I} \rangle$ [W/m^2] is the mean of the intensity values [62,106]. The change in speckle contrast can be calculated using $\Delta C = C_b - C$, where C_b [−] is the speckle contrast with no ultrasound. Provided that the exposure time (T) follows $1/(T\omega_a) \ll 1$, the speckle contrast can be calculated with $C \approx C_b/(1 + M)$ in which M is the modulation depth [62]. Exposure time needs to balance sufficient SNR while avoiding random speckle fluctuations due to Brownian motion [62]. See Fig. 6(a) for a generic system setup.

Resink et al. used speckle patterns to analyze the interactions of high intensity nanosecond laser pulses with tissue phantoms. One laser pulse was sent through a medium when the ultrasound wave reached a region of interest. A second pulse is sent when the ultrasound wave had propagated half a period, meaning it had shifted the phase by π. Acousto-optical signals were determined by comparing the intensities of the two speckle patterns. Additionally, the two pulses could be detected with one exposure time and the speckle pattern (C_2) compared to the speckle pattern (C_1) with one pulse such that $\Delta C = C_1 - C_2$ [63]. Theoretically, the fraction of tagged light could be calculated from the speckle patterns [64]. The authors used two pulses that were 27 ns apart for one ultrasound pulse. The system had an SNR of ~6 and an acquisition time of 40 ns. These parameters would be ideal for *in vivo* experiments of tissues with short decorrelation times. The energy and the pulse duration of the laser input would allow for PAT measurements and could easily be combined with a PAT system [65].

Resink and Steenbergen developed a theoretical model that determine the fraction of tagged light (R [−]) from speckle contrast images. They start by relating the phase modulation amplitude (δ_j [−]) with the fraction of tagged light. The electric field (E_j [V/m]) of the j path is $E_j = |E_j| e^{i\omega_0 t} e^{i[\varphi_j + \delta_j \sin(\omega_a t + \phi_j)]}$, in which ω_0 [Hz] is the angular frequency of light, t [s] is time, φ_j [−] is the phase of light, ω_a [Hz] is the ultrasound frequency, and ϕ_j [−] is the phase of the phase oscillation. The fraction of tagged light was

$$R = \left\langle \frac{\delta_n^2}{\delta_n^2 + 2} \right\rangle \approx \frac{1}{2} \langle \delta_n^2 \rangle, \tag{9}$$

under the assumption that $\delta_j \ll 1$. The model for the speckle contrast (c_{model}) used the summation of three statistically independent speckle patterns. The speckle pattern was assumed polarized, noise free, and with contrast close to unity. The contrast and fraction of tagged light were related with $R = 1 - c_{\text{model}}$ in which the tagged fraction was assumed to be small ($R \ll 1$) [64].

Zhu et al. used modulation depth measurements to observe effects of glucose concentrations of ultrasound modulated imaging. As glucose concentration increased in either intralipid or bovine hemoglobin solution, the modulation depth increased. However, the measurements were very sensitive to the temperature of the solution. Therefore, determining the difference between the physiologic changes and pathological changes of *in vivo* measurements presented a challenge [107].

3.2.2 Detecting ultrasound modulated light with incoherent light sources

As previously described the majority of the AOT signal originates from light that keeps its coherence as it travels through the medium. Incoherent light from AOT is much more difficult to detect. Regardless, there has been work done on detecting these weak incoherent signals.

Jarrett et al. demonstrated AOT with an incoherent LED light source (630 nm). By physically scanning a photomultiplier tube detector along the propagation of a continuous wave ultrasound beam, intensity signals were obtained that consisted of a pattern of maxima and minima. These patterns appeared to be projections of the variation of acoustic pressure in the medium. The ultrasound perturbation causes changes in density, which in turn causes changes in absorption within the medium. Phase shifts due to changes in index of refraction did not seem to play a part in the AOT signal. These signals could be observed in both clear (water) and turbid medium and could be useful to image sound fields directly [22].

Huynh et al. has employed ultrasound pulse sequences and harmonics to develop acousto-optical imaging techniques and observe incoherent signals. First, in a simple setup without the use of an external laser, they were able to image a chemiluminescent material embedded in a tissue phantom (μ_s'~30 μm). An ultrasound transducer was scanned across on surface of a phantom containing the chemiluminescent material and the signal from a photomultiplier tube was captured. The system resolved objects that are 5 mm apart at a 7 mm depth in a tissue phantom with a SNR ~80 [21]. This group also developed a numerical model to investigate ultrasound modulated bioluminescence tomography and understand its feasibility. They determined that the resulting ultrasound modulated bioluminescent signal would be caused by the variations in concentration of luciferase and not the alterations in optical properties due to density fluctuations or changes in refractive index. Therefore, they showed feasibility of bioluminescent imaging with AOT [66]. Also, Huynh et al. investigated the effect of a fluorescent

object's size on modulated light signals. Ultrasound modulation of fluorescent signals also produces an incoherent signal. If the object size is the same as the acoustic wavelength the detector will collect a constructive signal. However, if the object is an odd number of half wavelengths then there will be deconstructive interference. This interference effect is important to understand for fluorescent AOT since it will create image artifacts [23].

3.2.3 Interferometry and heterodyne digital holography to gain SNR or decrease acquisition time

Interferometry techniques have also been developed for acousto-optical imaging. In interferometry methods, a reference beam interferes with the light signal that had been transmitted through a sample [67]. For heterodyne digital holography, a source laser light is split into two beams in which one beam travels through the sample and the other becomes the reference beam (a.k.a. local oscillator). When performing acousto-optical imaging, the reference beam is either frequency shifted with an acousto-optic modulator to match the frequency of the modulated photons or has the same frequency as the signal input (Fig. 6(b)). If the reference beam has a similar frequency as the modulated light, then the beat frequency between the two will be low and interference between the beams will be easily detected, while the unmodulated light will provide a high beat frequency. The strength of the detected signal depends on the both the transmitted signal and reference beam. By increasing the reference beam intensity the overall signal will easily become shot-noise limited without any background amplification. Also, with this technique, the decorrelation noise can be filtered from the signal [108]. Gross proposed a theoretical model to relate how the untagged light, speckle noise, shot noise, decorrelation, and etendue affect the acousto-optical signal. Additionally, the model showed that the same detection sensitivity was achieved with or without decorrelation [109].

Using a custom-designed CMOS smart-pixel array, Barjean et al. developed a Fourier transform acousto-optic imaging (FT-AOI) system with interferometry detection. The sensor captured real-time analysis of the speckle pattern of the acousto-optic imaging. The system was capable of resolving objects along the ultrasound axis [68]. A full theoretical study of the methods had been developed [68] and assessed with the FT-AOI system [67]. This new method in acousto-optic imaging with axial resolution had improved SNR (~22). This approach uses a custom sensor with small etendue (24 × 24 pixels; 1 mm^2 area). The CMOS smart-pixel sensor had an integration time of 70 μs, which would be beneficial for *in vivo* imaging [67].

Lui et al. developed a heterodyne holography system that was adapted with a commercially available lock-in camera (300 × 300 pixels). The goal was to quickly create an alternating current (AC) map of the signal. The lock-in camera was set to the beat frequency between the signal and reference beam and captured the AC amplitude, which is proportional to the tagged light. The system was able to finish a measurement within 286 μs, which is within the correlation time of living biological tissue. However, there was poor axial resolution, due to long ultrasound bursts [69]. The advantage of this heterodyne holography systems is the fast acquisition times. The lock-in detection helps present the large background signal from being digitalized and can lead to a better utilization of the dynamic range compared to conventional heterodyne holography. Additionally, signals can be increased by adjusting the local oscillator, which would not have to undergo the safety limits that restrict the sample illumination beam. Also, with the proper setup, the decorrelation noise can be removed through filtering.

In the past, Fabry-Perot interferometers have been utilized for ultrasound modulated light detection [10,12]. To our knowledge, we have not found articles for this technique with AOT published since 2011. A challenge with these filters is that they are very sensitive to the light incidence angle.

3.2.4 Photorefractive crystal based detection to gain SNR, sensitivity, or imaging depth

Photorefractive based detection requires the use of a PRC that has a reference beam set to the frequency of either the modulated or unmodulated light. See Fig. 6(c) for the generic system setup. The reference beam interferes with the signal [70,110]. When the reference and signal beam interfere in the PRC, there is a small change in the index of refraction. Due to the photorefractive effect, the reference beam is diffracted within the crystal into the same wavefront and direction as the signal, which is also referred as two-wave mixing (see Fig. 7(a)) [52,110]. When the reference beam is the same frequency as the unmodulated signal, as in the absence of ultrasound, the reference and signal fields interfere constructively and exhibit the maximum detected signal. When ultrasound is employed there is a partial phase shift of the light, causing the reference and the signal to interfere less constructively, decreasing the detected signal [52]. Using their theoretical model, Gross et al. determined that the modulated signals for both the tagged and untagged detection schemes yielded signal strengths of similar magnitude [110].

Farahi et al. used two-wave mixing with a 1% tellurium-doped tin thiohypodiphosphate ($Sn_2P_2S_6$:Te) crystal. In their setup they were able to achieve an amplification factor of 24 and a response time of < 10 ms. The laser used for the imaging had a wavelength of 780 nm, which is within the tissue optical window. A multi-element ultrasound transducer was introduced to allow for 3D imaging of phantoms. The ultrasound probe was translated along one of the axes of the phantom. A photodiode was

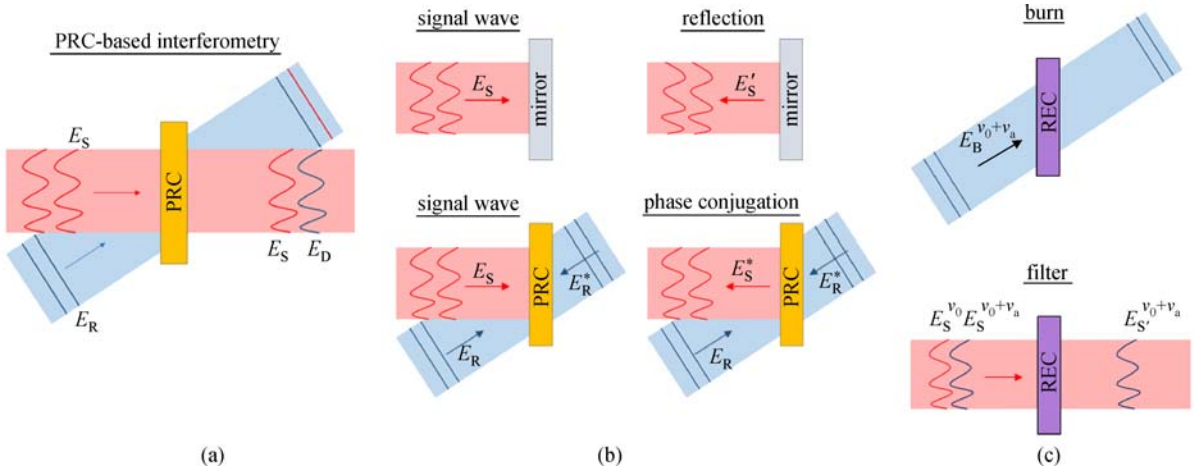

Fig. 7 Concepts behind the different crystals used in AOT. (a) Photorefractive crystal based interferometry: A reference beam (E_R) is set to a specific wavelength (i.e., frequency of the ultrasound modulated light) and travels through the photorefractive crystal (PRC) so that E_R is diffracted (E_D) and matches the wavefront of the signal wavefront (E_S) that has the same frequency as E_R. (b) Photorefractive crystal (PRC) phase conjugation. An example of an incident light wave (E_S) and how light is reflected off a mirror (E_S'). The wavefront reverses direction and the part of the light wave that arrived at the mirror first is reflected back first. For PRC-based phase conjugation, a reference beam (E_R) and its conjugate (E_R*) are injected into the PRC with an incident wave E_S moving to the left. The light wave is phase conjugated (E_S*) in which the shape of the wavefront is retained and moves to the left. However, only the portion of E_S that matches the frequency of E_R and E_R* will phase conjugated. (c) Spectral hole burning (SHB). For SHB, light of a specific frequency if filtered, while the rest of the light is absorbed by a rare-earth crystal (REC). The first step is to "burn" the crystal using a beam (E_B) with a given frequency. For example, the REC can be burned with the modulated light frequency (optical wavelength (ν_0) plus the ultrasound frequency (ν_a)). Ideally, only the signal that matches the frequency of E_B will pass through the REC and be detected

used to collect the signal. The 3D image took a few minutes to acquire [70]. To further increase the imaging speed, a system setup with a neodymium-doped vandate (ND:YVO_4) photorefractive crystal was created so that the response time of the crystal was 50 μs. Due to the low SNR, many readings needed to be averaged leading to a slow acquisition time. Additionally, the operation wavelength for the crystal was 1064 nm which is on the edge of the tissue optical window for biological tissue [71]. This shows the trade-off between factors such as speed and SNR. Using a $Bi_{12}SiO_{20}$ (BSO) crystal, the same group created a robust and stable system that does not employ a reference beam. An adaptive speckle correlation technique was used to perform phantom imaging. Imaging in a 40 mm phantom with absorptive inclusions had a contrast of 80% and a SNR of 30 [72]. A model and simulations of the self-referencing PRC setup were established to explain these results [73].

Laudereau et al. presented the first ultrasound modulated optical images of *ex vivo* liver samples. Their system uses two-wave mixing of a $Sn_2P_2S_6$:Te photorefractive crystal at 790 nm. The liver samples were embedded in a phantom and imaged. The acousto-optical imaging was able to locate regions in the samples that the ultrasound alone was not able to capture. Together with ultrasound imaging, this system could increase the sensitivity for tumor location and characterization. However, the optical properties have not been related to the imaging [74].

To push the depth that optical imaging can currently obtain, Lai et al. developed an ultrasound-modulated system that could image a phantom of an unprecedented 9.4 cm thickness within the safety limits for lasers and ultrasound. A high numerical aperture fiber bundle was used to capture the unmodulated light, which was filtered and amplified through a photorefractive BSO crystal. The modulated light signal was determined by subtracting the unmodulated light signals with and without ultrasound. Using this design in transmission setup, they were able to image through 9.4 cm thick phantom with optical inclusions at the half-way depth (4.7 cm). The ability to image through such thicknesses was attributed to the large collection etendue and a high two-wave mixing efficiency. To reach this depth, the axial resolution was rather poor due to long ultrasound pulses [13]. By using a large area photorefractive polymer [15,111] in their two-wave mixing setup, Suzuki et al. was able to increase the etendue by more than ten times. Additionally, the two-wave mixing of the polymer out-performed a BSO crystal with moderate light illumination (~190 mW/cm^2) and short ultrasound pulses. The set up was able to resolve absorptive objects within phantoms of 9.4 cm depth [15,16]. These polymers are, however, sensitive to changes in airflow, vibration, and temperature, making them challenging to use in practical applications. Also, they have a slow rise time (~20 s) which would not be ideal for *in vivo* imaging.

The biggest advantage of this technique has been the

unprecedented imaging depth that has been accomplished. Yet, the trade-off with imaging depth was axial resolution due to longer ultrasound pulses. The advances in PRCs have led to faster response times which could eventually be used in *in vivo* applications. For these *in vivo* applications to be practical, PRCs with operating wavelengths within the biologically relevant range need to be incorporated into AOT systems.

3.2.5 Phase conjugation with photorefractive crystals and polymers to improve imaging depth, SBR, etendue, or acquisition speed

Phase conjugation can focus light into highly scattering medium [75]. One of the limitations of phase conjugation is the necessity to image the optical field at two positions along the tissue surface, usually on both sides of the tissue. This issue could be resolved by either locally probing the field or placing the source within the medium. Particles (such as nanoparticles with nonlinear properties) could be utilized, this would be an invasive method in terms of medical imaging [112]. To overcome this limitation, the ultrasound focus in acousto-optical imaging can act as a guidestar and provides a non-invasive means for focused imaging. Therefore, combining AOT and phase conjugation in this way can enhance focusing depth within tissue [39].

Photorefractive crystals are capable of phase conjugation in a process called four-wave mixing. In four-wave mixing, there are two reference beams that are pumped into the crystal. If the two reference beams and the signal beam all have the same frequency then a phase conjugated wave of the same frequency traveling in the opposite direction of the signal beam will be generated (see Fig. 7(b)). Backward nondegenerate four-wave mixing uses a writing and reading sequence in which two beams of the same frequency create a hologram, while another beam of a different frequency reads the hologram. The phase conjugated beam has the same frequency as the reading beam, but its spatial structure may be influenced by the frequency difference of the reading and writing beams [113].

Xu et al. developed a system that combines ultrasound modulated light imaging with phase conjugation mirrors which allows for focusing of light inside scattering medium. The system setup has been dubbed time-reversed ultrasonically encoded (TRUE) optical focusing. Simply, the system has three main parts: a laser, ultrasound transducer, and a photorefractive crystal. The light travels through the medium and becomes encoded if the light passes through the ultrasound focus. From there, the encoded light is phase conjugated with a BSO crystal. The phase conjugation reverses its path, and the TRUE signal is detected by a photodetector (see Fig. 6(d)). They also demonstrated that if the phase conjugated signal converges to the ultrasonic focus then the square of the acousto-optical signal is proportional to their TRUE signal [75]. One of the limitations of the TRUE system had been the imaging depth in which some improvements were made. By adding an electro-optic modulator, the polarization of the laser light was controlled and the system was configured to have writing and reading modes. During the writing mode the "image" was being stored in the PRC. Once the polarization of the laser light input was changed, the reading mode let the "image" to be phase conjugated back through the sample and recorded using a photodiode. Adapting the modification to the TRUE system allowed light to improve focusing to a depth of 7 mm. Additionally, Wang's group also determined that the tightness of the focusing was determined by the ultrasonic focal zone [76]. A similar set up was used to retrieve reflection measurements. A light guide was placed on the same side as the input signal to capture reflected light. The reflected light was guided to the PRC and phase conjugated back toward the sample. A round-trip optical penetration thickness of about 16 mm was achieved ($\lambda = 532$; background $\mu_a = 0.02$ cm^{-2} and $\mu_s' = 20$ cm^{-1}) [77].

Due to the low modulated signal compared to the background unmodulated light, the focused optical energy needs to be increased. By using a photorefractive polymer instead of a PRC in the TRUE system, the etendue was increased which lead to a ~40 fold increase in the focused optical energy. This polymer worked with a 532 nm laser. The setup could image objects with an optical thickness of 120 scattering mean free paths. The polymer had a slow response time of about 5 s, which is not sufficiently fast for *in vivo* imaging due to the decorrelation time of biological tissue. Additionally, the signal was unstable after a long time (~30 min) and the polymer had a low optical damage threshold (~250 mW/cm^2) [78]. With a hybrid CW and pulse laser system, Ma et al. observed an unprecedented optical power gain of 33000 times (45 dB) for a target within scattering medium with their TRUE system setup. They use a BSO crystal that operates at 532 nm wavelength [114].

Lui et al. developed a faster TRUE system that imaged dynamic scattering medium with speckle correlation time as short as 5.6 ms. Additionally, they present the first focusing of light in living tissue (mouse ear). The system uses a $Sn_2P_2S_6$:Te PRC with an operating wavelength of ~790 nm, which is suitable for biological applications. Despite the impressive increase in speed, the imaging time needs to be further decreased in order to image thicker tissue that decorrelates faster due to blood flow [79]. Using a lock-in camera technique and SLMs, TRUE imaging was possible in low light signal-to-background ratio (SBR) conditions, with the wavefront measured as quickly as ~0.3 ms. As a result another limitation occurred in which it took about 30 ms to adjust the phase map on the SLM system and this became the determining factor in speed for the system [80].

Jang et al. developed a model to predict the penetration depth limit of TRUE imaging. The depth limit for a 800 nm

source with an ultrasound frequency of 10 MHz was a focusing depth of ~103 mm in a medium with an absorption coefficient of μ_a = 0.005 mm^{-1} and reduced scattering coefficient of μ_s' = 0.17 mm^{-1}. When the frequency was decreased to 5 MHz focusing depth was ~139 mm. While with a 532 nm source the focusing depth ~34 mm, since this wavelength gets absorbed much more in biological tissue [18].

To increase the speed of acousto-optical imaging, Jayet et al. tested a system with a ND:YVO_4 PRC which has an emission lifetime of 100 μs at 1064 nm. With their setup, phase conjugation was achieved with a gain of up to 1000. Therefore, with high amplification of the signal, the sensitivity of AOT imaging was increased and with faster response time, speckle decorrelation could be avoided [115].

3.2.6 Focused fluorescent excitation beyond one mean free path to gain resolution and SNR

Fluorescence imaging can be used to tag molecular markers or cells, but has had very limited high-resolving imaging depth due to highly scattering nature of biological tissue. Focused excitation of fluorescence has been limited to about one transport mean path (~1 mm) [82]. With the development of AOT techniques, focused fluorescent excitation deep with tissue may be possible. Fluorescent imaging was briefly mentioned before as an incoherent light source [23]. In the following work, ultrasound modulated light was used to create a guidestar so that light can be focused into a specific point (ultrasound focus) within the medium to excite fluorophores in that region.

Wang's group developed fluorescent imaging with optical focusing in thick turbid media using their TRUE system configured with a BSO crystal at 532 nm. The TRUE system creates a guide-star for dynamic focusing. The signal beam travels through the medium where it is tagged with ultrasound. The outgoing wave was then phase conjugated back into the medium where the light was focused back to the ultrasound focus location and excited the fluorescent target (see Fig. 6(f)) [83]. With this configuration they were able to obtain fluorescent imaging at a depth greater than 4 transport mean free paths with a resolution comparable to the size of the ultrasound focus (~1 mm). Their analog PRC-based TRUE system required 200 ms for recording and 10 ms for reading and was admittedly too slow for *in vivo* biomedical measurements [83].

Tay et al. developed a method for wavefront shaping using ultrasonically encoded light to capture fluorescent intensities by combining SLM-based illumination and PRC-based detection. The SLM configuration was iteratively modified based on the light detected from a single photodiode. They were able to achieve an 11-fold increase in signal after 600 iterations (1 magnitude increase after 370 iterations). This method was thereby too slow for *in vivo* applications. Yet, the diffuse light in a turbid media was refocused into an ultrasound focus with a focus-to-background ratio (FBR) of more than one magnitude [84]. To increase speed, Suzuki et al. replaced the PRC with a SLM in their TRUE system, which was setup for florescent imaging in reflection mode. Iterative focusing of SLMs is time consuming and could not be utilized for biomedical application. Instead of iterative focusing, the ultrasound focus was gradually moved and the SLM wavefront from the previous recording was used to generate the next recording. They observed that as the step size of the scanning decreased, the focus signal peak increased, as well as the SNR. This continuous scanning scheme improved SNR and decreased scanning time [85].

Fluorescent ultrasound-modulated optical imaging with digital phase conjugation was also employed by Si et al. [81]. Digital phase conjugation requires the use of SLMs and computer setup (see Fig. 6(e)). Precisely synchronized light and ultrasound pulses were used to probe the medium. A SLM was used to reflect the light back through the sample. The digital phase conjugation provided sufficient gain to cause a suitable level of excitation in the fluorescent beads. The signal was captured with a fluorescent detector. The contrast was calculated by using the difference between the signal with and without the SLM pattern shifted from its focused position divided by the background signal. They demonstrated fluorescent imaging beyond the ballistic regime with a lateral resolution of less than 40 μm [81]. In a dual digital phase conjugation setup fluorescence system, a beam of light was passed back and forth through an ultrasound focus. With each iteration of the beam passing there was an increase in resolution and FBR. This group observed a ~3 fold increase in resolution and a ~5 fold increase in FBR in 2 mm thick phantoms [86].

One challenge that Wang et al. realized was the undesired background illumination caused by partial phase conjugation. Complete phase conjugations is infeasible, but to address some of the challenges that the background illumination caused, they developed a fluorescence imaging TRUE system that combines digital phase conjugation and dynamic wavefront shaping. Briefly, the modulated light from the sample interferes with an equally frequency-shifted reference beam and was imaged with a CMOS camera. The phase map was determined from the interference pattern on the camera. The SLM reflects the reference beam with the conjugate of the recorded phase map. During this playback mode the reference beam intensity was increased by a factor of 5 ×10^5, which gives the light enough power to excite the fluorophore to provide a detectable signal. The light travels back to the location of the ultrasound focus where the fluorophore would be excited. The fluorescence outside the ultrasound focus was also excited which causes a background signal that can be subtracted by digitally manipulating the phase of the illuminating field. The spatial resolution was similar to that

of the ultrasound focus dimensions and the system imaged at a depth of 2.5 mm in biological tissue. The imaging time per pixel was 6.7 s. The laser power was about 10 mW/mm^2, which would be above the safety limit for the wavelength used (532 nm) [82].

To overcome the spatial resolution of the TRUE system, time-reversal of variance encoded (TROVE) was developed by Judkewitz et al. The TROVE light system combined wavefront shaping with ultrasound-modulated light techniques. For this technique, light wavefronts were passed through an ultrasound focus and the encoded light wavefronts were detected. This process was repeated for many random wavefronts. The output of the random wavefronts was used to compute and provide another input wavefront that was displayed on the SLM. As the light propagates back through the sample, the light formed a speckle-sized optical focus, which improved the spatial resolution. The group saw a ~6 fold improvement in resolution compared to TRUE. The TRUE system had a focus width of 31.1 μm which was on the order of the ultrasound focus (~30 μm). The TROVE system had a focus width of 5.2 μm which was on the order of the size of the optical speckle for the setup (~5 μm). Additionally, there was a ~20 fold increase in the intensity of the peak signal intensity. The imaging time was 2 h for a 30 μm × 30 μm image [87].

Another method was developed by Ruan et al., called Iterative TRUE (iTRUE) light focusing. iTRUE used the signal source for subsequent phase conjugations procedures and can be configured for reflection measurements. In other words, the signal from the sample was detected, processed, and phase conjugated with an SLM. The process was repeated for the same spot to increase the focusing of the light and increase SNR. The light intensity of the fluorescent signal at the focus was increased ~20 fold and the spatial resolution was improved ~2 and ~3 fold in the axial and lateral directions, respectively [88].

3.2.7 Quantum memory techniques: spectral hole burning of rare earth crystals and atomic frequency combs

Another method for AOT is quantum memory techniques that utilize rare earth crystals. The crystals can be manipulated to provide several functions to facilitate an interesting AOT approach with the use of pump beams to change the index of refraction and absorption spectrum. When light of the resonance wavelength (ν_L) approaches an atom in the crystal, it may cause the atom to change its energy state. Once the atom relaxes back to its original energy state, it releases a photon of the same wavelength and phase. Therefore, the change in excitation states of the atom causes the photon to "slow down", but only at a given frequency [116]. To initiate this process, there needs to be a preparation phase where the crystal goes through a "burning" sequence. If a laser beam of frequency, ν_L, is illuminated at high power on a cryogenically cooled absorbing rare earth crystal, the resonant ions become excited causing a depletion of the ground state for the resonance line. The burning sequence causes a change in absorption in a narrow laser linewidth, which in turn causes a change in index of refraction. This process is called spectral hole burning (SHB). At ν_L, the crystal becomes transparent with a linewidth corresponding to the laser linewidth, typically in the sub-megahertz range, while wavelengths outside this linewidth are absorbed. This creates a very narrow band transmission bandpass filter with high contrast. Therefore, the small side band of the ultrasound modulated signal could be filtered while suppressing the large background unmodulated signal [117,118] (see Fig. 7(c)). See Fig. 6(g) for generic setup. Li et al. theoretically determined the intensity of the transmitted signal through the SHB medium in which the transmitted signal intensity was

$$I_{s,\mathrm{out}} = I_s(\omega_s)\exp\left\{-2Re\left[\int_0^{L_C}\alpha(\omega_s,\omega_\mathrm{p},z)\mathrm{d}z\right]\right\}, \quad (10)$$

where $I_s(\omega_s)$ [W/m^2] is the input intensity at optical angular frequency ω_s [Hz], L_c [m] is the crystal length, ω_P [Hz] is the pump frequency, α [m^{-1}] is the absorption of the crystal, and z [m] is the position. Speckles can be processed in parallel due to the large etendue of the crystal [118]. With a double pass pumping configuration, Xu et al. were able to obtain deeper spectral hole burning with a change in a TM:YAG (793 nm) crystal absorption of $\Delta\alpha(\omega_P) = 0.13$. The double pass pumping was achieved by reflecting the pump beam back through the crystal. The strong doping concentration of the crystal led to an increase in the spectral hole width, but did not affect the imaging. The two main limitations of the experiment was that the optical power was limited by the laser used and that the window of the cryostat limited the etendue of the system [89].

Zhang et al. combined high performance spectral hole burning and slow light to see 9 cm into a tissue phantom ($\mu_s' = 10$ cm^{-1}) with no detectable background. A PR:YSO crystal was employed which has an operating wavelength of 606 nm and a long hole lifetime. The signal was observed as a function of time (microsecond scale) and the delayed light signals could be observed. They report a 30 dB suppression of the untagged background. Additionally, they calculated the optimal parameters for their system (higher etendue, higher laser power, more efficient photon counter) within safety standards and estimated that imaging 18 cm tissue phantoms could be possible [14].

McAuslan et al. used an atomic frequency comb (AFC) combined with balanced heterodyne detection for acousto-optical imaging. AFC do not require magnetic or electrical pumping, only optical. There were two AFCs centered to plus and minus the ultrasound frequency from the frequency of the laser input. They were able to detect the ultrasound modulated signal with a 49 dB discrimination between the sidebands and carrier signal [90]. To mimic

interactions with biological tissue, a highly scattered laser beam (606 nm) was used by focusing the beam on unpolished aluminum surface. To our understanding, they do not image samples under ultrasound modulation for this study. They also report a 7 dB improvement of the SNR from the carrier frequency [90] over the SHB method with acousto-optical imaging, previously described [14]. Using the same setup, the highly scattering beam setup had a ~29 dB detector limited discrimination of the side bands compared to the carrier frequency [91]. The AFC technique was demonstrated in tissue phantoms, where a 1-D of photon echoes were obtained in the axial direction [92].

3.3 Acousto-optical coherence tomography to improve spatial resolution

Lesaffre et al. applied stochastic phase modulation to both the light and ultrasound. By using the time delay (τ) between the ultrasound and the light modulation, the zone along the ultrasound axis can be selected. The time delay was set to $\tau = z/c_{us}$ where z is the selected location and c_{us} was the speed of the ultrasound within the medium. This technique is similar to finding depth in OCT and thus has been dubbed acousto-optical coherence tomography (AOCT). Light and ultrasound were continuously applied but underwent the same random phase jumps (0 and π) with a time delay for the laser light (see Fig. 6(h)). They were able to achieve millimeter resolution [93].

They also developed a theoretical model for AOCT with random phase jumps and a tagged light photorefractive signal with PRCs. Their model included lock-in detection of the modulation frequency which was in the kHz range. Lesaffre et al. demonstrated that the tagged light field was proportional to the amplitude of the input optical field, the acoustic power of the ultrasound transducer, and their time correlation function. Additionally, they showed that modulated photorefractive detected signal was proportional to the optical intensity, the surface area of the photodiode, the acoustic power, the square of their time correlation function, and the phase modulation of the input signal $(1-2r)H(t)$, where r [–] is the duty cycle and $H(t)$ [–] is the phase modulation [94].

They experimentally validated their theoretical model and were able to record images with different axial resolutions. Their axial resolution (Δz) was dependent on the characteristic time of the random phase jumps, $T\varphi$, in which $\Delta z = c_{us}T\varphi$. Currently this method uses a wavelength (1064 nm) that makes probing deep into tissue difficult, but other PRCs that have operating wavelengths optimal for biological tissue could be employed. Additionally, the acoustic safety requirements are not fulfilled (720 mW/cm^2 average acoustic power), but could be used with long ultrasound pulses instead of continuous to obtain safety standards [95]. The AOCT technique was applied using digital holography instead of photorefractive detection. A La Guillaume et al. was able to implement the technique with 1 mm resolution and used a 780 nm laser. They also showed that the SNR was 3 times better with the AOCT compared to the ultrasound burst technique. Their system did not satisfy medical safety standards [96].

3.4 Combined with photoacoustics to obtain fluence measurements

PAT has a similar setup to AOT in the sense that both imaging techniques require a laser source and an ultrasound transducer. One group has combined PAT and acousto-optical imaging in order to improve PAT measurements. Staley et al. developed PAT guided ultrasound wavefront shaping to assist acousto-optical imaging. PAT was used to probe the medium and used to determine a new ultrasound wavefront that will compensate for speed of sound (SOS) aberrations. The SOS variations in ultrasound focusing causes undesirable effects in acousto-optical imaging. Parallel speckle detection was obtained for acousto-optical measurements with pulsed ultrasound and stroboscopic illumination. The guided focusing technique showed better focusing in the presence of SOS variation compared to unguided PAT focusing [97]. Also, Daoudi et al. developed techniques utilizing acousto-optical imaging to compensate for fluence variations in PAT signals. They were able to correct fluence measurements due to variations within an accuracy of 5% [98]. Their analytical model was able to relate the acousto-optic signal to the local fluence in the scattered medium. Using the model and experimental measurements, the acousto-optically measured fluence closely matched the locally measured fluence in the scattered medium. Also, this method could be combined with PAT imaging to reduce artifacts caused by fluence variations [19]. Using these techniques, Hussain et al. combined acousto-optical imaging and PAT imaging to determine oxygenation in blood samples. The acousto-optical setup was used to determine local fluence to compensate the PAT measurements. Additionally, they developed an analytical model for calculating oxygen saturation based on these measurements. They demonstrated that the combined system was able to resolve the oxygen concentration better than PAT alone [99].

3.5 Commercial devices for blood flow measurements

Despite the challenges that AOT has, there has been a commercial device that has been used for several human clinical trials. The CerOx (Ornim Medical Ltd.) device was composed of a laser source, ultrasound transducer, and detector that were setup on the same side of the tissue for reflection measurements [119]. There were three light wavelengths between 780 and 830 nm. The ultrasound frequency was 1 MHz. The source and detector were

placed 12 mm apart and can probe volumes of 1 cm^3 [100]. The ultrasound modulated light was detected by a single photodetector. They use the cross correlation between the light intensity and the ultrasound pulse to determine blood flow. As blood flow increased, the amplitude of the cross correlation decreased [119,120]. There have been several human clinical studies using this device. Some of the recent studies involved comparing UT-NIRS with ^{133}XE-SPECT [100], monitoring brain oxygenation in patients with severe brain injury [121], monitoring administration of anesthesia [122], and monitoring cerebral autoregulation in cardiac surgery patients [123,124].

Currently their main product has been c-FLOW™ which has both FDA and CE approval. The purpose of the device is to monitor blood flow to the brain, while it also but can be used for monitoring microcirculatory blood flow in other parts of the body [101]. The c-FLOW system uses near-infrared light (808 nm) modulated by a 1 MHz ultrasound. The system measures the cerebral flow index in arbitrary units and can image at a 2 cm depth. Dynamic measurements are taken every 2 – 3 s [102]. Since the focus was to capture signals from the brain, contamination of the signal from the superficial flow of blood in previously used techniques needed to be reduced. A technique to acquire depth sensitive techniques was established and incorporated into the c-FLOW system. Spectral analysis of the modulated signal was used. The spectral width would be broader the more the phase of the light was changed. Instead of continuous ultrasound, pulses were used which propagate through the medium and are located at different depths at different times. To get the location and amplitude of the flow patterns, the differential spectral width was used. The differential spectral width was created by subtracting the spectral width from adjacent layers [37]. Using these techniques, Tsalach et al. combined their c-FLOW system with a blood pressure unit to observe the mean arterial pressure and cerebral blood flow congruently in real time [102].

These systems are capable to of dynamically recording ultrasound-modulated signals in brain tissue at NIR wavelengths. However, the devices are limited to 2 cm depths and applications such as tumor diagnosis or monitoring would be limited. Also, the measurements obtained are relative blood flow measurements that do not yield any molecular information about the tissue.

4 Reconstruction algorithms and determining optical properties

In DOT, light is highly scattering in biological tissue and requires detectors placed at several locations along the surface of the medium to capture where the light exits the medium for image reconstruction. The solution for extracting optical properties from these measurements of scattered medium is often highly ill-posed. The additional information that AOT provides can substantially decrease the ill-posed nature of reconstruction algorithms compared to traditional optical tomography. Here, we present an overview of the type of techniques that have been developed by different groups without elaborate derivation or detail.

Powell and Leung used an alternative method with a time-domain model of the acousto-optical signal for AOT reconstructions. For the forward model the diffusion approximation was modified for ultrasound perturbation. They used a linear reconstruction algorithm to obtain the absorption map of a medium of known background absorption. The reconstructions were used for single source detector measurements of the autocorrelation field of AOT [125]. They continued to develop techniques in which a nonlinear reconstruction method was created to recover both the absorption and scattering coefficients for 2D images. Multiple source and detector pairs were used in order to restore uniqueness to the problem. The damped Gauss-Newton method was employed [126]. Since traditional Newton-based methods are computationally intensive and require sufficient memory, Powell et al. developed an adjoint-assisted gradient based image reconstruction method. The method was capable of both 2D and 3D reconstructions and determined both absorption and scattering coefficients [127].

Bal and Schotland developed a reconstruction algorithm based on the inverse problem of the diffusion equation to obtain the diffusion and absorption coefficient from incoherent measurements of modulated light. Additionally, the ultrasound was not assumed to be focused and presumed interferometry measurements were not used [128]. The work was further developed to an iterative algorithm to solve a system of partial differential equations [129]. Other algorithms such as the solution to the hybrid inverse source problem have been used to reconstruct density of luminescent source for acousto-optic bioluminescence tomography using the diffusion equation [130] and radiative transport equation [131].

Ammari et al. developed a reconstruction algorithm to obtain the absorption coefficient. Boundary measurements of the light signal, when the medium was unperturbed and perturbed by spherical US waves, were cross-correlated and used in the algorithm. They establish equations using spherical Radon transform inversion and the diffusion model. Then the nonlinear coupled system was solved iteratively to obtain the absorption coefficient [132]. The algorithm was additionally generalized for piecewise smooth optical absorption distributions [133]. Physiological features in biological tissue are not smooth or piecewise, as was previously assumed [132,133]. Continuing the work on these previous algorithms [132,133], Ammari et al. developed a method to reconstruct discontinuous parameter distributions [134].

Huynh et al. proposed a maximum likelihood algorithm to reconstruct pulsed AOT signals along the ultrasound

axis [135]. Allmaras and Bangerth created a coupled system of equations using the diffusion approximation and the autocorrelation function (G) for the measure signal. They developed a simple iterative reconstruction algorithm to obtain the absorption coefficient from the medium. They achieved both good stability and resolution that would not be possible in typical optical tomography [136].

The diffusion approximation was modified by Bratchenia et al. for modulated light. They added this modification to their model-based inversion reconstruction algorithm. In their model they only consider the variation in absorption. This method was able to determine the location and absorption of embedded absorbers in a phantom [137].

Varma et al. were able to acquire the amplitude of vibration in the ultrasound focus with their reconstruction algorithm. Using modulation depth measurements, reconstructions were performed using an Gauss-Newton scheme to solve for the inverse problem together with the diffusion approximation for the forward model [138]. The modulation depth is dependent on the stiffness of the material, so AOT could be used to determine Young's Modulus of the tissue [138,139]. Thereby, a reconstruction algorithm to determine Young's Modulus from modulation depth measurements was also developed [139].

Since the location within the medium for the modulated light is known (i.e., ultrasound focus), experimental setups for line scans of a sample can be designed. Then reconstruction techniques similar to X-ray CT may be utilized. Li and Wang first demonstrated this tomographic method involving filtered back-projection algorithm by coupling linear scans with the ultrasound and rotating the sample to obtain different projections [140]. As described previously (Section 3.1.4), filtered back-projection methods were used to reconstruct acousto-optical images by scanning planar ultrasound waves within a sample [51].

While there have been several algorithms developed for AOT, there have been few groups to employ such techniques for their experiments [51]. Due to the focusing nature of AOT, images of phantoms have been relatively easy to extract, albeit without the optical properties. This task becomes significantly more complicated in biological media in which the absorbing regions are not known and may interact with tagged light between the ultrasound focus and the detector. Therefore, the use of reconstruction techniques will be important, but has not significantly come into play with most current techniques.

5 Discussion and highlights of the field

There are several common challenges that the AOT field has encountered while designing systems for *in vivo* imaging, such as improving resolution, reducing acquisition time, increasing contrast or SNR, increasing etendue, integrating relevant wavelengths for biological tissue, incorporating safety limitations, resolving optical and mechanical properties, and increasing imaging depth.

The resolution of AOT is dependent on the ultrasound parameters and is similar to the ultrasound focus dimensions [75,87,112]. The axial resolution (direction of ultrasound propagation) is generally larger than then the lateral resolution. To improve axial resolution, acoustic bursts have been employed which is a common technique in echography [96], but at the cost of SNR [21]. Lateral resolution can also be improved with higher ultrasound frequency [21], but would lead to shallower focusing depth of the ultrasound. There were two studies that were able to overcome ultrasound resolution limitation. First was the TROVE (Section 3.2.6) system that had a resolution similar to the optical speckle size (~5 μm). However, the acquisition time was very long and could not be used for biomedical applications [87]. The other system was TRUME (Section 3.1.6), which utilized microbubbles to achieve a spatial resolution of ~2 μm [53]. Both these studies were taken with ultrasound frequencies between 20 and 50 MHz and imaged samples that were < 1 cm^3 [53,87].

Acquisition speed is also an important parameter to allow for real-time imaging or to avoid the effects of decorrelation. Experimental measurements for decorrelation times of objects such as milk, an arm, or a fingertip were 1 ms or less [62]. Imaging times must be less than the decorrelation time in order to avoid noise. Acquisition time for PRC-based interferometry (Section 3.2.4) may be limited by the response time of the crystals. Crystal response time can range between 1 and 100 ms, while Nd:YVO_4 has been shown to have a response time of 100 μs and may be applicable to avoid decorrelation artifacts [115]. SLMs configurations are also currently limited to the speed that the phase map can be shaped (~0.1 s) [41]. With acquisition time > 1 s for SLM setups (Section 3.2.6), biomedical applications would not be possible due to decorrelation time of tissue [41,80–82,84,87,88]. Heterodyne digital holography (Section 3.2.3) has had the fastest acquisition times in which one group achieved an integration time of 70 μs for their custom-made detector [67] and another group acquired one measurement within 286 μs [69]. The fastest system that was found in our review (Section 3.2.1) had a 40 ns imaging time and used nanosecond light pulses to determine speckle contrast [65].

Contrast and SNR are determined by the amount of modulated light that can be detected compared to the background signal of the unmodulated light. The modulated light signal is significantly less than the unmodulated light signal, which is the crux of the challenges for optimal AOT system design. Often when developing these techniques there was a trade-off between SNR and another parameters. For example, to get a better SNR, multiple scans can be completed and averaged, but this increases

acquisition time [71] (see Section 3.2.4) or to obtain deep tissue imaging at sufficient SNR, but with poor axial resolution [13] (see Section 3.2.4).

Moreover, in order to obtain sufficient SNR, maximizing the etendue of the detection of modulated light is very important for the imaging biological tissue [14,90]. SBH crystals (Section 3.2.7) have some of the highest etendue compared to other techniques [14]. However, due to the cryostat windows, the etendues are comparable with that of PRC. Photorefractive polymer can have etendue as high as ~400 mm·sr, but are highly sensitive to environmental noise and had a slow rise time [15,16].

To obtain clear speckle patterns, lasers with a coherence length of 7 cm or more is needed. This requirement has led to the use of 532 nm (Nd:YAG) lasers [12]. Most of the experiments from our literature search (see Section 3) have used 532 nm light sources [13,15,16,19,36,42–45,49,53,54,56–60,63,65,69,72,75–78,80,82–84,87,88,97–99,105,114]. Others have looked at 1064 nm wavelengths [46,52,71,93,115] or between 606 and 638 nm [14,23,48,90–92,107], which is on the very edge of the relevant wavelengths for biological imaging. Last, there have been some studies have looked in the 778 – 793 nm range [41,51,67,70,74,79,81,86,89,96,117,118]. To our knowledge, there have not been studies within the 800 – 1000 nm range. In order for deep tissue *in vivo* imaging to be possible, system development must include more appropriate wavelengths.

With AOT, safety must be considered in both terms of laser and ultrasound exposure. These safety limitations must be taken into consideration for *in vivo* experiments and eventual human imaging. However, safety levels were not always discussed within the literature, which granted is not necessary for phantom experiments. Nevertheless, if AOT will be used for *in vivo* applications these limitation must be adapted.

There have been several studies that were able to accomplish imaging through 9 cm thick tissue phantoms. First, was the BSO PRC-based interferometer system [13] (Section 3.2.4), followed by a similar system using photorefractive polymer [15,16]. Additionally, there was study with SBH (Section 3.2.7) that acquired 9 cm depth imaging with 30 dB suppression of the untagged background [14]. These are unprecedented imaging depths.

Despite the promise of 18 cm imaging depths, there has only been one study we have found in our literature search AOT with SHB (Section 3.2.7) since 2011 [14]. This technique has several advantages over the previously mentioned ones. First, SHB techniques have the highest etendue compared to other techniques, such as photorefractive methods [10,14]. Second, SHB is not sensitive to the decorrelation time of biological tissue [10,117]. The SHB scheme does require cryogenic cooling of the crystal [10,117], but due to the relatively small crystal size this would be more manageable than, for example, the cooling system required for a magnetic resonance imaging system.

AOT can determine not only the optical properties of tissue, but also the mechanical properties. Currently, reconstruction algorithms (Section 4) are necessary to determine absorption [125–127,132–134,136,137] or scattering coefficient [126,127]. One group did use two different pressure (Section 3.1.2) waves to determine scattering coefficient of the medium without reconstructions [46,47]. Regardless, AOT imaging has shown qualitative images of relative absorption, but just has not related these absorption maps to the quantitative values. Last, mechanical properties such as elasticity [58,59], viscosity [58], and Young's Modulus [42,139] have also been determined (Sections 3.1.1, 3.1.7, and 4).

As previously mentioned in Section 4, the effect of heterogeneous tissue for AOT needs to be better understood. For AOT, heterogeneity can be expressed in two ways: optical and mechanical. If the mechanical properties of the tissue change then the acousto-optical signal will change due to the difference in pressure amplitude at the ultrasound focus. This effect has been seen in some of a phantom study previously mentioned, although the reason for the increase in signal due to increase elasticity was unclear [59]. Optical and mechanical heterogeneity will have to be taken into account as the field progresses.

6 Future direction and conclusion

Several different techniques have been developed to produce sufficient AOT methods for biomedical imaging applications. AOT has also benefitted from other research in the ultrasound field, development of PRCs and PRPs, advancements of SLMs and cameras, as well as other fields. Determining which of these techniques has more merit than others would be a difficult task, since each technique contributes to overcoming one or a few of the key challenges of AOT. Not overcoming all these challenges at once has prevented the field from moving as fast as its counterpart, PAT. The breakthroughs in AOT have led to greater understanding on how to move forward and what challenges we still face. There is also the opportunity that AOT can outperform other optical techniques in terms of imaging depth [11,14]. If these imaging depths are achieved, new applications could be realized (i.e. heart imaging). Although AOT development has been a relatively slow progression, there are untapped possibilities. Once AOT can accomplish *in vivo* imaging, new opportunities and interest can be placed on understanding biological processes.

While many of these advancements have been made within the last five to six years in the acousto-optic biological imaging field, there still remains a great deal of work to be done to viably create a system for biological imaging at large depths. Specifically, there needs to be systems designed at relevant wavelengths for deep tissue *in vivo* imaging with the possibility of multi-wavelength

design to calculate physiologic parameters such as oxygenation saturations. Second, safety levels of both the optical and ultrasound components must be completely taken into account. Third, decorrelation of the biological tissue must be addressed whether with decorrelation insensitive system design, faster PRC-based detection schemes, or other techniques that may develop in the near future. With these developments, deep tissue imaging with non-ionizing radiation and high molecular sensitivity may be achieved.

Acknowledgements This work was supported by the Science Foundation Ireland. The authors would like to thank Andreas Walther, Lars Rippe, Mats Gustafsson and Stefan Kröll for their useful discussions.

Acronyms

AFC – atomic frequency comb

AOCT – acousto-optical coherence tomography

AOT – acousto-optical tomography

ARF – acoustic radiation force

BSO- $Bi_{12}SiO_{20}$

CNR – contrast-to-noise ratio

CUDAMCML – Compute Unified Device Architecture Monte Carlo for multi layered tissue

DA- diffusion approximation

DOT – diffuse optical tomography

FBR – focus-to-background ratio

FDTD – finite difference time domain

FT-AOI – Fourier transform acousto-optic imaging

GPU – graphics processing unit

HIFU – high intensity focused ultrasound

iTRUE – iterative time-reversed ultrasonically encoded

MC – Monte Carlo

MI – mechanical index

OCT – optical coherence tomography

PAT – photoacoustic tomography

PCS – pressure contrast signal

PRC – photorefractive crystal

SBR – signal-to-background ratio

SHB – spectral hole burning

SLM – spatial light modulator

SNR – signal-to-noise ratio

SOS – speed of sound

SW-LASCA – shear-wave laser speckle contrast analysis

TROVE – time-reversal of variance encoded

TRUE – time-reversed ultrasonically encoded

TRUME – time-reversed ultrasound microbubble encoded

References

1. Wang L V. Ultrasound-mediated biophotonic imaging: a review of acousto-optical tomography and photo-acoustic tomography. Disease Markers, 2003– 2004, 19(2–3): 123–138
2. Brillouin L.Diffusion de la lumière et des rayons X par un corps transparent homogène. Influence de l'agitation thermique. Ann. Physique (Paris), 1922, 17(88–122): 21
3. Debye P, Sears F W. On the scattering of light by supersonic waves. Proceedings of the National Academy of Sciences of the United States of America, 1932, 18(6): 409–414
4. Lucas R, Biquard P. Propriétés optique des milieux solides et liquides soumis aux vibrations élastiques ultra sonores. Journal of Physics, 1932, 71(10): 464–477
5. Marks F A, Tomlinson H W, Brooksby G W. Comprehensive approach to breast cancer detection using light: photon localization by ultrasound modulation and tissue characterization by spectral discrimination. In: Proceedings of SPIE 1888, Photon Migration and Imaging in Random Media and Tissues. 1993, 500–510
6. Wang L, Jacques S L, Zhao X. Continuous-wave ultrasonic modulation of scattered laser light to image objects in turbid media. Optics Letters, 1995, 20(6): 629–631
7. Leutz W, Maret G. Ultrasonic modulation of multiply scattered light. Physica B, Condensed Matter, 1995, 204(1 – 4): 14–19
8. Wang L V. Mechanisms of ultrasonic modulation of multiply scattered coherent light: an analytic model. Physical Review Letters, 2001, 87(4): 043903
9. Li C, Kim C, Lihong V W. Photoacoustic tomography and ultrasound-modulated optical tomography. In: Boas D A, Pitris C, Ramanujam N, eds. Handbook of Biomedical Optics. Boca Raton, Florida: CRC Press, 2011, 419–442
10. Resink S G, Boccara A C, Steenbergen W. State-of-the art of acousto-optic sensing and imaging of turbid media. Journal of Biomedical Optics, 2012, 17(4): 040901
11. Walther A, Rippe L, Lihong V W, Andersson-Engels S, Kröll S. Is optical imaging of oxygenation at heart depth possible? (submitted), 2017
12. Elson D S, Li R, Dunsby C, Eckersley R, Tang M X. Ultrasound-mediated optical tomography: a review of current methods. Interface Focus, 2011, 1(4): 632–648
13. Lai P, Xu X, Wang L V. Ultrasound-modulated optical tomography at new depth. Journal of Biomedical Optics, 2012, 17(6): 066006
14. Zhang H, Sabooni M, Rippe L, Kim C, Kröll S, Wang L V, Hemmer P R. Slow light for deep tissue imaging with ultrasound modulation. Applied Physics Letters, 2012, 100(13): 131102
15. Suzuki Y, Lai P, Xu X, Wang L. High-sensitivity ultrasound-modulated optical tomography with a photorefractive polymer. Optics Letters, 2013, 38(6): 899–901
16. Lai P, Suzuki Y, Xu X, Wang L V. Exploring ultrasound-modulated optical tomography at clinically useful depths using the photorefractive effect. In: Oraevsky A A, Wang L V, eds. Photons Plus Ultrasound: imaging and Sensing: Proceedings of SPIE. 2013, 85812X
17. Yao G, Wang L V. Theoretical and experimental studies of

ultrasound-modulated optical tomography in biological tissue. Applied Optics, 2000, 39(4): 659–664

18. Jang M, Ruan H, Judkewitz B, Yang C. Model for estimating the penetration depth limit of the time-reversed ultrasonically encoded optical focusing technique. Optics Express, 2014, 22(5): 5787–5807
19. Hussain A, Daoudi K, Hondebrink E, Steenbergen W. Mapping optical fluence variations in highly scattering media by measuring ultrasonically modulated backscattered light. Journal of Biomedical Optics, 2014, 19(6): 066002
20. Wang L V. Mechanisms of ultrasonic modulation of multiply scattered coherent light: a Monte Carlo model. Optics Letters, 2001, 26(15): 1191–1193
21. Huynh N T, Hayes-Gill B R, Zhang F, Morgan S P. Ultrasound modulated imaging of luminescence generated within a scattering medium. Journal of Biomedical Optics, 2013, 18(2): 020505
22. Jarrett C W, Caskey C F, Gore J C. Detection of a novel mechanism of acousto-optic modulation of incoherent light. PLoS One, 2014, 9(8): e104268
23. Huynh N T, Ruan H, He D, Hayes-Gill B R, Morgan S P. Effect of object size and acoustic wavelength on pulsed ultrasound modulated fluorescence signals. Journal of Biomedical Optics, 2012, 17(7): 076008
24. Wang L V, Wu H. Biomedical Optics: Principles and Imaging. New Jersey: John Wiley & Sons, 2012
25. Sakadžić S, Wang L V. Ultrasonic modulation of multiply scattered coherent light: an analytical model for anisotropically scattering media. Physical Review E: Statistical, Nonlinear, and Soft Matter Physics, 2002, 66(2): 026603
26. Yao G, Wang L V. Signal dependence and noise source in ultrasound-modulated optical tomography. Applied Optics, 2004, 43(6): 1320–1326
27. Sakadžić S, Wang L V. Correlation transfer equation for ultrasound-modulated multiply scattered light. Physical Review E: Statistical, Nonlinear, and Soft Matter Physics, 2006, 74(3): 036618
28. Sakadžić S, Wang L V. Correlation transfer equation for multiply scattered light modulated by an ultrasonic pulse. Journal of the Optical Society of America. A, Optics, Image Science, and Vision, 2007, 24(9): 2797–2806
29. Sakadžić S, Wang L V. Modulation of multiply scattered coherent light by ultrasonic pulses: an analytical model. Physical Review E: Statistical, Nonlinear, and Soft Matter Physics, 2005, 72(3): 036620
30. Alerstam E, Svensson T, Andersson-Engels S. Parallel computing with graphics processing units for high-speed Monte Carlo simulation of photon migration. Journal of Biomedical Optics, 2008, 13(6): 060504
31. Leung T S, Powell S.Fast Monte Carlo simulations of ultrasound-modulated light using a graphics processing unit. Journal of Biomedical Optics, 2010, 15(5): 055007
32. Powell S, Leung T S. Highly parallel Monte-Carlo simulations of the acousto-optic effect in heterogeneous turbid media. Journal of Biomedical Optics, 2012, 17(4): 045002
33. Adams M T, Cleveland R O, Roy R A. Modeling-based design and assessment of an acousto-optic guided high-intensity focused ultrasound system. Journal of Biomedical Optics, 2017, 22(1): 017001
34. Lu M Z, Wu Y P, Shi Y, Guan Y B, Guo X L, Wan M X. Monte Carlo simulation of scattered light with shear waves generated by acoustic radiation force for acousto-optic imaging. Chinese Physics Letters, 2012, 29(12): 124302
35. Li Y J, Huang W J, Ma F C, Wang R, Lu M Z, Wan M X. A modified Monte Carlo model of speckle tracking of shear wave induced by acoustic radiation force for acousto-optic elasticity imaging. Chinese Physics Letters, 2016, 33(11): 114301
36. Li S, Cheng Y, Song L, Eckersley R J, Elson D S, Tang M X. Tracking shear waves in turbid medium by light: theory, simulation, and experiment. Optics Letters, 2014, 39(6): 1597–1600
37. Tsalach A, Schiffer Z, Ratner E, Breskin I, Zeitak R, Shechter R, Balberg M. Depth selective acousto-optic flow measurement. Biomedical Optics Express, 2015, 6(12): 4871–4886
38. Tsalach A, Metzger Y, Breskin I, Zeitak R, Shechter R. Ultrasound modulated light blood flow measurement using intensity auto-correlation function: a Monte-Carlo simulation. In: Proceedings of SPIE 8943, Photons Plus Ultrasound: Imaging and Sensing, 2014, 89433N
39. Hollmann J L, Horstmeyer R, Yang C, DiMarzio C A. Analysis and modeling of an ultrasound-modulated guide star to increase the depth of focusing in a turbid medium. Journal of Biomedical Optics, 2013, 18(2): 025004
40. Hollmann J L, Horstmeyer R, Yang C, DiMarzio C A. Diffusion model for ultrasound-modulated light. Journal of Biomedical Optics, 2014, 19(3): 035005
41. Fiolka R, Si K, Cui M. Parallel wavefront measurements in ultrasound pulse guided digital phase conjugation. Optics Express, 2012, 20(22): 24827–24834
42. Chandran R S, Roy D, Kanhirodan R, Vasu R M, Devi C U. Ultrasound modulated optical tomography: Young's modulus of the insonified region from measurement of natural frequency of vibration. Optics Express, 2011, 19(23): 22837–22850
43. Chandran R S, Devaraj G, Kanhirodan R, Roy D, Vasu R M. Detection and estimation of liquid flow through a pipe in a tissue-like object with ultrasound-assisted diffuse correlation spectroscopy. Journal of the Optical Society of America A, Optics, Image Science, and Vision, 2015, 32(10): 1888–1897
44. Chandran R S, Sarkar S, Kanhirodan R, Roy D, Vasu R M. Diffusing-wave spectroscopy in an inhomogeneous object: local viscoelastic spectra from ultrasound-assisted measurement of correlation decay arising from the ultrasound focal volume. Physical Review E: Statistical, Nonlinear, and Soft Matter Physics, 2014, 90(1): 012303
45. Yang Q, Xu X, Lai P, Xu D, Wang L V. Time-reversed ultrasonically encoded optical focusing using two ultrasonic transducers for improved ultrasonic axial resolution. Journal of Biomedical Optics, 2013, 18(11): 110502
46. Lai P, Roy R A, Murray T W. Quantitative characterization of turbid media using pressure contrast acousto-optic imaging. Optics Letters, 2009, 34(18): 2850–2852

47. Murray T W, Lai P, Roy R A. Measuring tissue properties and monitoring therapeutic responses using acousto-optic imaging. Annals of Biomedical Engineering, 2012, 40(2): 474–485
48. Ruan H, Mather M L, Morgan S P. Pulse inversion ultrasound modulated optical tomography. Optics Letters, 2012, 37(10): 1658–1660
49. Ruan H, Mather M L, Morgan S P. Pulsed ultrasound modulated optical tomography with harmonic lock-in holography detection. Journal of the Optical Society of America A, Optics, Image Science, and Vision, 2013, 30(7): 1409–1416
50. Ruan H, Mather M L, Morgan S P. Pulsed ultrasound modulated optical tomography utilizing the harmonic response of lock-in detection. Applied Optics, 2013, 52(19): 4755–4762
51. Laudereau J B, Grabar A A, Tanter M, Gennisson J L, Ramaz F. Ultrafast acousto-optic imaging with ultrasonic plane waves. Optics Express, 2016, 24(4): 3774–3789
52. Lai P, McLaughlan J R, Draudt A B, Murray T W, Cleveland R O, Roy R A. Real-time monitoring of high-intensity focused ultrasound lesion formation using acousto-optic sensing. Ultrasound in Medicine & Biology, 2011, 37(2): 239–252
53. Ruan H, Jang M, Yang C. Optical focusing inside scattering media with time-reversed ultrasound microbubble encoded light. Nature Communications, 2015, 6: 8968
54. Ruan H, Mather M L, Morgan S P. Ultrasound modulated optical tomography contrast enhancement with non-linear oscillation of microbubbles. Quantitative Imaging in Medicine and Surgery, 2015, 5(1): 9–16
55. Liu Y, Feshitan J A, Wei M Y, Borden M A, Yuan B. Ultrasound-modulated fluorescence based on fluorescent microbubbles. Journal of Biomedical Optics, 2014, 19(8): 085005
56. Li R, Elson D S, Dunsby C, Eckersley R, Tang M X. Effects of acoustic radiation force and shear waves for absorption and stiffness sensing in ultrasound modulated optical tomography. Optics Express, 2011, 19(8): 7299–7311
57. Cheng Y, Li R, Li S, Dunsby C, Eckersley R J, Elson D S, Tang M X. Shear wave elasticity imaging based on acoustic radiation force and optical detection. Ultrasound in Medicine & Biology, 2012, 38 (9): 1637–1645
58. Cheng Y, Li S, Eckersley R J, Elson D S, Tang M X. Viscosity measurement based on shear-wave laser speckle contrast analysis. Journal of Biomedical Optics, 2013, 18(12): 121511
59. Cheng Y, Li S, Eckersley R J, Elson D S, Tang M X. Detecting tissue optical and mechanical properties with an ultrasound modulated optical imaging system in reflection detection geometry. Biomedical Optics Express, 2015, 6(1): 63–71
60. Li S, Cheng Y, Eckersley R J, Elson D S, Tang M X. Dual shear wave induced laser speckle contrast signal and the improvement in shear wave speed measurement. Biomedical Optics Express, 2015, 6(6): 1954–1962
61. Li J, Wang L V. Methods for parallel-detection-based ultrasound-modulated optical tomography. Applied Optics, 2002, 41(10): 2079–2084
62. Bratchenia A, Molenaar R, Kooyman R P H. Towards quantitative acousto-optic imaging in tissue. Laser Physics, 2011, 21(3): 601–607
63. Resink S G, Hondebrink E, Steenbergen W. Towards acousto-optic tissue imaging with nanosecond laser pulses. Optics Express, 2014, 22(3): 3564–3571
64. Resink S G, Steenbergen W. Tandem-pulsed acousto-optics: an analytical framework of modulated high-contrast speckle patterns. Physics in Medicine and Biology, 2015, 60(11): 4371–4382
65. Resink S, Hondebrink E, Steenbergen W. Solving the speckle decorrelation challenge in acousto-optic sensing using tandem nanosecond pulses within the ultrasound period. Optics Letters, 2014, 39(22): 6486–6489
66. Zhang Q, Mather M L, Morgan S P. Numerical investigation of the mechanisms of ultrasound-modulated bioluminescence tomography. IEEE Transactions on Bio-medical Engineering, 2015, 62(9): 2135–2143
67. Barjean K, Contreras K, Laudereau J B, Tinet É, Ettori D, Ramaz F, Tualle J M. Fourier transform acousto-optic imaging with a custom-designed CMOS smart-pixels array. Optics Letters, 2015, 40(5): 705–708
68. Barjean K, Ramaz F, Tualle J M. Theoretical study of Fourier-transform acousto-optic imaging. Journal of the Optical Society of America A, Optics, Image Science, and Vision, 2016, 33(5): 854–862
69. Liu Y, Shen Y, Ma C, Shi J, Wang L V. Lock-in camera based heterodyne holography for ultrasound-modulated optical tomography inside dynamic scattering media. Applied Physics Letters, 2016, 108(23): 231106
70. Farahi S, Benoit E, Grabar A A, Huignard J P, Ramaz F. Time resolved three-dimensional acousto-optic imaging of thick scattering media. Optics Letters, 2012, 37(13): 2754–2756
71. Jayet B, Huignard J P, Ramaz F. Fast wavefront adaptive holography in Nd:YVO_4 for ultrasound optical tomography imaging. Optics Express, 2014, 22(17): 20622–20633
72. À La Guillaume E B, Bortolozzo U, Huignard J P, Residori S, Ramaz F. Dynamic ultrasound modulated optical tomography by self-referenced photorefractive holography. Optics Letters, 2013, 38(3): 287–289
73. Devaux F, Huignard J P, Ramaz F. Modelization and optimized speckle detection scheme in photorefractive self-referenced acousto-optic imaging. Optics Express, 2014, 22(9): 10682–10692
74. Laudereau J B, À La Guillaume E B, Servois V, Mariani P, Grabar A A, Tanter M, Gennisson J L, Ramaz F. Multi-modal acousto-optic/ultrasound imaging of *ex vivo* liver tumors at 790 nm using a $Sn_2P_2S_6$ wavefront adaptive holographic setup. Journal of Biophotonics, 2015, 8(5): 429–436
75. Xu X, Liu H, Wang L V. Time-reversed ultrasonically encoded optical focusing into scattering media. Nature Photonics, 2011, 5 (3): 154–157
76. Liu H, Xu X, Lai P, Wang L V. Time-reversed ultrasonically encoded optical focusing into tissue-mimicking media with thickness up to 70 mean free paths. Journal of Biomedical Optics, 2011, 16(8): 086009
77. Lai P, Xu X, Liu H, Suzuki Y, Wang L V. Reflection-mode time-reversed ultrasonically encoded optical focusing into turbid media. Journal of Biomedical Optics, 2011, 16(8): 080505
78. Suzuki Y, Xu X, Lai P, Wang L V. Energy enhancement in time-

reversed ultrasonically encoded optical focusing using a photorefractive polymer. Journal of Biomedical Optics, 2012, 17(8): 080507

79. Liu Y, Lai P, Ma C, Xu X, Grabar A A, Wang L V. Optical focusing deep inside dynamic scattering media with near-infrared time-reversed ultrasonically encoded (TRUE) light. Nature Communications, 2015, 6: 5904
80. Liu Y, Ma C, Shen Y, Wang L V. Bit-efficient, sub-millisecond wavefront measurement using a lock-in camera for time-reversal based optical focusing inside scattering media. Optics Letters, 2016, 41(7): 1321–1324
81. Si K, Fiolka R, Cui M. Fluorescence imaging beyond the ballistic regime by ultrasound pulse guided digital phase conjugation. Nature Photonics, 2012, 6(10): 657–661
82. Wang Y M, Judkewitz B, Dimarzio C A, Yang C. Deep-tissue focal fluorescence imaging with digitally time-reversed ultrasound-encoded light. Nature Communications, 2012, 3: 928
83. Lai P, Suzuki Y, Xu X, Wang L V. Focused fluorescence excitation with time-reversed ultrasonically encoded light and imaging in thick scattering media. Laser Physics Letters, 2013, 10(7): 075604
84. Tay J W, Lai P, Suzuki Y, Wang L V. Ultrasonically encoded wavefront shaping for focusing into random media. Scientific Reports, 2014, 4(1): 3918
85. Suzuki Y, Tay J W, Yang Q, Wang L V. Continuous scanning of a time-reversed ultrasonically encoded optical focus by reflection-mode digital phase conjugation. Optics Letters, 2014, 39(12): 3441–3444
86. Si K, Fiolka R, Cui M. Breaking the spatial resolution barrier via iterative sound-light interaction in deep tissue microscopy. Scientific Reports, 2012, 2: 748
87. Judkewitz B, Wang Y M, Horstmeyer R, Mathy A, Yang C. Speckle-scale focusing in the diffusive regime with time-reversal of variance-encoded light (TROVE). Nature Photonics, 2013, 7(4): 300–305
88. Ruan H, Jang M, Judkewitz B, Yang C. Iterative time-reversed ultrasonically encoded light focusing in backscattering mode. Scientific Reports, 2014, 4(1): 7156
89. Xu X, Kothapalli S-R, Liu H, Wang L V. Spectral hole burning for ultrasound-modulated optical tomography of thick tissue. Journal of Biomedical Optics, 2010, 15(6): 066018
90. McAuslan D, Taylor L, Longdell J. Using quantum memory techniques for optical detection of ultrasound. Applied Physics Letters, 2012, 101(19): 191112
91. Taylor L R, McAuslan D L, Longdell J J. Optical detection of ultrasound using AFC-based quantum memory technique in cryogenic rare earth ion doped crystals. In: Proceedings of SPIE 8581, Photons Plus Ultrasound: Imaging and Sensing. 2013, 858117
92. Taylor L R, Doronin A, Meglinski I, Longdell J J. Acousto-optic imaging using quantum memories in cryogenic rare earth ion doped crystals. In: Proceedings of SPIE 8943, Photons Plus Ultrasound: Imaging and Sensing. 2014, 89431D
93. Lesaffre M, Farahi S, Gross M, Delaye P, Boccara C, Ramaz F. Acousto-optical coherence tomography using random phase jumps on ultrasound and light. Optics Express, 2009, 17(20): 18211–18218
94. Lesaffre M, Farahi S, Boccara A C, Ramaz F, Gross M. Theoretical study of acousto-optical coherence tomography using random phase jumps on ultrasound and light. Journal of the Optical Society of America A, Optics, Image Science, and Vision, 2011, 28(7): 1436–1444
95. Lesaffre M, Farahi S, Ramaz F, Gross M. Experimental study of z resolution in acousto-optical coherence tomography using random phase jumps on ultrasound and light. Applied Optics, 2013, 52(5): 949–957
96. A La Guillaume E B, Farahi S, Bossy E, Gross M, Ramaz F. Acousto-optical coherence tomography with a digital holographic detection scheme. Optics Letters, 2012, 37(15): 3216–3218
97. Staley J, Hondebrink E, Peterson W, Steenbergen W. Photoacoustic guided ultrasound wavefront shaping for targeted acousto-optic imaging. Optics Express, 2013, 21(25): 30553–30562
98. Daoudi K, Hussain A, Hondebrink E, Steenbergen W. Correcting photoacoustic signals for fluence variations using acousto-optic modulation. Optics Express, 2012, 20(13): 14117–14129
99. Hussain A, Petersen W, Staley J, Hondebrink E, Steenbergen W. Quantitative blood oxygen saturation imaging using combined photoacoustics and acousto-optics. Optics Letters, 2016, 41(8): 1720–1723
100. Schytz H W, Guo S, Jensen L T, Kamar M, Nini A, Gress D R, Ashina M. A new technology for detecting cerebral blood flow: a comparative study of ultrasound tagged NIRS and 133Xe-SPECT. Neurocritical Care, 2012, 17(1): 139–145
101. c-FLOW^{TM} - Cerebral Perfusion Monitor- Ornim- Non Invasive Brain Monitoring | Brain Blood Flow | Cerebral Blood Flow, http://www.ornim.com/c-flow/.
102. Tsalach A, Ratner E, Lokshin S, Silman Z, Breskin I, Budin N, Kamar M. Cerebral autoregulation real-time monitoring. PLoS One, 2016, 11(8): e0161907
103. Zhu L, Xie W, Li Z, Li H. Experimental study of ultrasound-modulated scattering light using different frequencies ultrasound probes. Chinese Optics Letters, 2014, 12(7): 071701–071703
104. Cui M, Yang C. Implementation of a digital optical phase conjugation system and its application to study the robustness of turbidity suppression by phase conjugation. Optics Express, 2010, 18(4): 3444–3455
105. Singh M S, Kanhirodan R, Vasu R M, Roy D. Ultrasound modulation of coherent light in a multiple-scattering medium: experimental verification of nonzero average phase carried by light. Biomedical Optics Express, 2012, 3(9): 2100–2110
106. Li J, Ku G, Wang L V. Ultrasound-modulated optical tomography of biological tissue by use of contrast of laser speckles. Applied Optics, 2002, 41(28): 6030–6035
107. Zhu L, Lin J, Lin B, Li H. Noninvasive blood glucose measurement by ultrasound-modulated optical technique. Chinese Optics Letters, 2013, 11(2): 021701–021705
108. Gross M, Goy P, Al-Koussa M. Shot-noise detection of ultrasound-tagged photons in ultrasound-modulated optical imaging. Optics Letters, 2003, 28(24): 2482–2484
109. Gross M. Speckle decorrelation in ultrasound-modulated optical tomography made by heterodyne holography. 2016, arXiv preprint arXiv:1606.02902,
110. Gross M, Ramaz F, Forget B, Atlan M, Boccara A, Delaye P,

Roosen G. Theoretical description of the photorefractive detection of the ultrasound modulated photons in scattering media. Optics Express, 2005, 13(18): 7097–7112

111. Tay S, Blanche P A, Voorakaranam R, Tunç A V, Lin W, Rokutanda S, Gu T, Flores D, Wang P, Li G, St Hilaire P, Thomas J, Norwood R A, Yamamoto M, Peyghambarian N. An updatable holographic three-dimensional display. Nature, 2008, 451(7179): 694–698
112. Lerosey G, Fink M. Acousto-optic imaging: Merging the best of two worlds. Nature Photonics, 2013, 7(4): 265–267
113. He G S. Optical phase conjugation: principles, techniques, and applications. Progress in Quantum Electronics, 2002, 26(3): 131–191
114. Ma C, Xu X, Wang L V. Analog time-reversed ultrasonically encoded light focusing inside scattering media with a 33000× optical power gain. Scientific Reports, 2015, 5(1): 8896
115. Jayet B, Huignard J P, Ramaz F. Optical phase conjugation in Nd: YVO_4 for acousto-optic detection in scattering media. Optics Letters, 2013, 38(8): 1256–1258
116. Khurgin J B. Slow light in various media: a tutorial. Advances in Optics and Photonics, 2010, 2(3): 287–318
117. Li Y, Zhang H, Kim C, Wagner K H, Hemmer P, Wang L V. Pulsed ultrasound-modulated optical tomography using spectral-hole burning as a narrowband spectral filter. Applied Physics Letters, 2008, 93(1): 011111
118. Li Y, Hemmer P, Kim C, Zhang H, Wang L V. Detection of ultrasound-modulated diffuse photons using spectral-hole burning. Optics Express, 2008, 16(19): 14862–14874
119. Racheli N, Ron A, Metzger Y, Breskin I, Enden G, Balberg M, Shechter R. Non-invasive blood flow measurements using ultrasound modulated diffused light. In: Proceedings of SPIE 8223, Photons Plus Ultrasound: Imaging and Sensing. 2012, 82232A
120. Ron A, Racheli N, Breskin I, Metzger Y, Silman Z, Kamar M, Nini A, Shechter R, Balberg M. Measuring tissue blood flow using ultrasound modulated diffused light. In: Proceedings of SPIE 8223, Photons Plus Ultrasound: Imaging and Sensing. 2012, 82232J
121. Rosenthal G, Furmanov A, Itshayek E, Shoshan Y, Singh V. Assessment of a noninvasive cerebral oxygenation monitor in patients with severe traumatic brain injury. Journal of Neurosurgery, 2014, 120(4): 901–907
122. Schwarz M, Rivera G, Hammond M, Silman Z, Jackson K, Kofke W A. Acousto-optic cerebral blood flow monitoring during induction of anesthesia in humans. Neurocritical Care, 2016, 24 (3): 436–441
123. Hori D, Hogue C, Adachi H, Max L, Price J, Sciortino C, Zehr K, Conte J, Cameron D, Mandal K. Perioperative optimal blood pressure as determined by ultrasound tagged near infrared spectroscopy and its association with postoperative acute kidney injury in cardiac surgery patients. Interactive Cardiovascular and Thoracic Surgery, 2016, 22(4): 445–451
124. Hori D, Hogue C W Jr, Shah A, Brown C, Neufeld K J, Conte J V, Price J, Sciortino C, Max L, Laflam A, Adachi H, Cameron D E, Mandal K. Cerebral autoregulation monitoring with ultrasound-tagged near-infrared spectroscopy in cardiac surgery patients. Anesthesia and Analgesia, 2015, 121(5): 1187–1193
125. Powell S, Leung T S. Linear reconstruction of absorption perturbations in coherent ultrasound-modulated optical tomography. Journal of Biomedical Optics, 2013, 18(12): 126020
126. Powell S, Leung T S. Quantitative reconstruction of absorption and scattering coefficients in ultrasound-modulated optical tomography. In: Proceedings of SPIE 8943, Photons Plus Ultrasound: Imaging and Sensing. 2014, 89434X–89434X–89411
127. Powell S, Arridge S R, Leung T S. Gradient-based quantitative image reconstruction in ultrasound-modulated optical tomography: first harmonic measurement type in a linearised diffusion formulation. IEEE Transactions on Medical Imaging, 2016, 35 (2): 456–467
128. Bal G, Schotland J C. Inverse scattering and acousto-optic imaging. Physical Review Letters, 2010, 104(4): 043902
129. Bal G, Moskow S. Local inversions in ultrasound-modulated optical tomography. Inverse Problems, 2014, 30(2): 025005
130. Bal G, Schotland J C. Ultrasound-modulated bioluminescence tomography. Physical Review E: Statistical, Nonlinear, and Soft Matter Physics, 2014, 89(3): 031201
131. Bal G, Chung F J, Schotland J C. Ultrasound modulated bioluminescence tomography and controllability of the radiative transport equation. SIAM Journal on Mathematical Analysis, 2016, 48(2): 1332–1347
132. Ammari H, Bossy E, Garnier J, Nguyen L, Seppecher L. A reconstruction algorithm for ultrasound-modulated diffuse optical tomography. Proceedings of the American Mathematical Society, 2014, 142(9): 3221–3236
133. Ammari H, Garnier J, Nguyen L H, Seppecher L. Reconstruction of a piecewise smooth absorption coefficient by an acousto-optic process. Communications in Partial Differential Equations, 2013, 38(10): 1737–1762
134. Ammari H, Nguyen L H, Seppecher L. Reconstruction and stability in acousto-optic imaging for absorption maps with bounded variation. Journal of Functional Analysis, 2014, 267 (11): 4361–4398
135. Huynh N T, He D, Hayes-Gill B R, Crowe J A, Walker J G, Mather M L, Rose F R, Parker N G, Povey M J, Morgan S P. Application of a maximum likelihood algorithm to ultrasound modulated optical tomography. Journal of Biomedical Optics, 2012, 17(2): 026014
136. Allmaras M, Bangerth W. Reconstructions in ultrasound modulated optical tomography. Journal of Inverse and Ill-Posed Problems, 2011, 19(6): 801–823
137. Bratchenia A, Molenaar R, van Leeuwen T G, Kooyman R P H. Acousto-optic-assisted diffuse optical tomography. Optics Letters, 2011, 36(9): 1539–1541
138. Varma H M, Mohanan K P, Hyvönen N, Nandakumaran A K, Vasu R M. Ultrasound-modulated optical tomography: recovery of amplitude of vibration in the insonified region from boundary measurement of light correlation. Journal of the Optical Society of America A, Optics, Image Science, and Vision, 2011, 28(11): 2322–2331
139. Mohanan K P, Nandakumaran A K, Roy D, Vasu R M. Ultrasound-modulated optical tomography: direct recovery of elasticity distribution from experimentally measured intensity autocorrelation. Journal of the Optical Society of America A, Optics, Image

Science, and Vision, 2015, 32(5): 955–963

140. Li J, Wang L V. Ultrasound-modulated optical computed tomography of biological tissues. Applied Physics Letters, 2004, 84(9): 1597–1599

Dr. **Jacqueline Gunther** received her B.E. degree in Biomedical Engineering from Stony Brook University, USA in 2011. In 2013 and 2015, she received her M.S. and M.Phil degrees, respectively, both in Biomedical Engineering from Columbia University, USA. Her Ph.D. work involved using diffuse optical tomography to monitor breast cancer patients undergoing neoadjuvant chemotherapy and develop methods to predict response to treatment. In 2016, she received her Ph.D. degree in Biomedical Engineering from Columbia University. Also, in 2016 she joined the Biophotonics Group at Tyndall National Institute, University College Cork, Ireland as post-doctoral researcher. Her work involves fundamental research of light propagation in biological media and acousto-optical tomography.

Prof. **Stefan Andersson-Engels** is Head of Biophotonics at Tyndall National Institute, University College Cork, Ireland and was appoi-nted there in 2016. Andersson-Engels graduated in Engineering Physics from Lund University in 1985, and received his Ph.D. degree in Physics from Lund University 1990. He was then a postdoc at McMaster University in Ontario, Canada 1990 – 1991. After a few years as lecturer he was appointed professor in 1999 at Lund University. Dr. Andersson-Engels has published extensively in the area of biomedical optics, with 200 papers in peer-reviewed journals and an H-index of 60 (Google Scholars). His main interest is fundamental and translational research in biophotonics. He is presently setting up a new biophotonics laboratory at Tyndall, with a number of translational project in collaboration with clinicians and industrial partners. The more fundamental aspects of the research is toward developing biophotonics tools for deep tissue imaging, including acousto-optical tomography and how to best employ upconverting nanoparticles as a contrast agent. Other areas of general interest are optical spectroscopy and photodynamic therapy. He is presently also active in two start-up companies in the field of biomedical optics.